Two-length-scale turbulence model for self-similar buoyancy-, shock-, and shear-driven mixing

Brandon E. Morgan, Oleg Schilling, and Tucker A. Hartland

Phys. Rev. E **97**, 013104 — Published 10 January 2018

DOI: 10.1103/PhysRevE.97.013104

Two-length-scale turbulence model for self-similar buoyancy-, shock-, and shear-driven mixing

Brandon E. Morgan, Oleg Schilling, and Tucker A. Hartland*
Lawrence Livermore National Laboratory
Livermore, California 94550

(Dated: December 21, 2017)

The three-equation k-L-a turbulence model [B. Morgan and M. Wickett, "Three-equation model for the self-similar growth of Rayleigh–Taylor and Richtmyer–Meshkov instabilities," Phys. Rev. E **91** (2015)] is extended by the addition of a second length scale equation. It is shown that the separation of turbulence transport and turbulence destruction length scales is necessary for simultaneous prediction of the growth parameter and turbulence intensity of a Kelvin–Helmholtz shear layer when model coefficients are constrained by similarity analysis. Constraints on model coefficients are derived that satisfy an ansatz of self-similarity in the low-Atwood-number limit and allow the determination of model coefficients necessary to recover expected experimental behavior. The model is then applied in one-dimensional simulations of Rayleigh–Taylor, reshocked Richtmyer–Meshkov, Kelvin–Helmholtz, and combined Rayleigh–Taylor/Kelvin–Helmholtz instability mixing layers to demonstrate that the expected growth rates are recovered numerically. Finally, it is shown that model behavior in the case of combined instability is to predict a mixing width that is a linear combination of Rayleigh–Taylor and Kelvin–Helmholtz mixing processes.

I. INTRODUCTION

Canonical Rayleigh–Taylor (RT) instability occurs when two fluids of differing densities are subject to an acceleration vector that opposes in direction the mean density gradient [1, 2]. Richtmyer–Meshkov (RM) instability occurs when two fluids of differing densities are subject to acceleration from a shock wave [3–5]. RT and RM instability processes are of fundamental importance in a host of turbulent mixing applications including supersonic combustion [6], astrophysical phenomena [7], and inertial confinement fusion (ICF) [8]. Kelvin–Helmholtz (KH) instability is a shear-driven instability mechanism that occurs between two fluids with different parallel components of velocity [9, 10]. In many physical systems, including oceanic and atmospheric flows [11–14], stratified mixing layers exist in the presence of free shear flow, leading to a combined RT/KH mixing process. In ICF applications, when a shock interacts with a material interface obliquely, it is expected that the normal component should generate RM instability while the parallel component should generate KH instability [15, 16]. It is therefore important in many engineering applications to be able to accurately model the simultaneous effects of buoyancy and shear.

While much experimental [17–29] and computational [30–49] work exists studying RT, RM, and KH instabilities in isolation, fewer studies have been performed to investigate combined RT/KH or RM/KH instability. Recent experimental studies by Akula and collaborators [50–52] have investigated the dynamics of the combined RT/KH instability in a wind tunnel at Atwood numbers ranging from 0.04 to 0.73. Work has also been performed recently at the National Ignition Facility (NIF) [53] and on the OMEGA laser [54] to provide data on shear-dominated RM/KH instability in the high energy density physics (HEDP) regime. Olson *et al.* [55] have additionally investigated the combined RT/KH instability in the early nonlinear regime using large-eddy simulation (LES).

As it is not always practical to run LES or direct numerical simulations (DNS), there remains a need for reduced-order modeling of turbulent mixing due to the simultaneous effects of buoyancy and shear. Reynolds-averaged Navier–Stokes (RANS) models, by construction, are best suited to the prediction of fully developed turbulence and, therefore, mixing layer growth in the nonlinear regime. The k-L-a model has been previously shown to accurately predict canonical RT and RM growth when model coefficients are set to satisfy an ansatz of self-similarity [56].

The present work extends the k-L-a model to additionally predict the growth of free shear flow. The approach of Schwarzkopf *et al.* [57] to evolve two different length scales characterizing turbulence transport and destruction separately is adopted. It will be demonstrated that when model coefficients are set according to the derived constraints, self-similar solutions exist for the evolution of RT and KH mixing layers, and when a second length scale equation is used, it is possible to simultaneously match the experimental growth parameter and turbulence intensity of a free shear layer. While the Schwarzkopf (or BHR 3.1) model solves model transport equations for each component of the Reynolds stress tensor as well as for the density-specific-volume covariance b, it will be shown with the present model that these complexities are not essential to match buoyancy- or shear-driven mixing

* Present address: University of California, Merced, California 95340

layer evolution.

This paper is organized as follows. First, in Section II, the two-length-scale k-L-a model (henceforward referred to as the k-2L-a model) is presented. In Section III, similarity analysis is utilized to determine constraints on model coefficients necessary to reproduce expected RT, RM, and KH growth parameters. The model is applied in quasi-one-dimensional (quasi-1D) simulations of canonical RT, RM, KH, and combined RT/KH mixing layers in Section IV. Finally, in Section V, conclusions are drawn, and recommendations are made concerning the direction of future work.

II. MODEL EQUATIONS

The k-2L-a model is derived from the compressible RANS equations for a multi-component, non-reactive gas mixture. In the present work, an overbar denotes Reynolds averaging, and a tilde denotes mass-weighted (Favre) averaging. An arbitrary scalar, f, is decomposed as

$$f = \overline{f} + f' = \widetilde{f} + f'' \,, \tag{1}$$

where the Favre average is related to the Reynolds average through the density, ρ, according to

$$\widetilde{f} = \frac{\overline{\rho\, f}}{\overline{\rho}} \,. \tag{2}$$

The Reynolds stress tensor, mass-flux velocity vector, and density–specific-volume covariance are defined, respectively, in terms of the velocity vector, u_i, and the specific volume, $v \equiv 1/\rho$, by

$$\overline{\rho}\,\tau_{ij} \equiv -\overline{\rho\, u_i'' \, u_j''} \,, \tag{3a}$$

$$a_i \equiv -\overline{u_i''} \,, \tag{3b}$$

$$b \equiv -\overline{\rho'\, v'} \,. \tag{3c}$$

Equations (4)–(11) below summarize the k-2L-a model, where t is time, x_i is the spatial dimension vector, g_i is the gravitational acceleration vector, p is the static pressure, e is the specific internal energy, Y_α is the scalar mass fraction of component α, k is the turbulence kinetic energy, L_t is the turbulent transport length scale, L_d is the turbulent destruction length scale, and μ_t is the eddy viscosity. The covariance b is closed in Eq. (14) using component partial densities, ρ_α, and volume fractions, V_α. The model coefficients C_μ, C_a, C_B, C_D, C_{L1}, C_{L2t}, C_{L2d}, N_a, N_e, N_k, N_{Lt}, N_{Ld}, N_Y, and C_{dev} will be set through similarity analysis. The model equations are

$$\frac{D\overline{\rho}}{Dt} = -\overline{\rho}\,\frac{\partial \widetilde{u}_i}{\partial x_i} \,, \tag{4}$$

$$\overline{\rho}\,\frac{D\widetilde{Y}_\alpha}{Dt} = \frac{\partial}{\partial x_i}\left(\frac{\mu_t}{N_Y}\,\frac{\partial \widetilde{Y}_\alpha}{\partial x_i}\right) \,, \tag{5}$$

$$\overline{\rho}\,\frac{D\widetilde{u}_j}{Dt} = \overline{\rho}\, g_j - \frac{\partial \overline{p}}{\partial x_j} + \frac{\partial}{\partial x_i}\left(\overline{\rho}\,\tau_{ij}\right) \,, \tag{6}$$

$$\begin{aligned}\overline{\rho}\,\frac{D\widetilde{e}}{Dt} =& -\overline{p}\,\frac{\partial \widetilde{u}_i}{\partial x_i} - a_i\,\frac{\partial \overline{p}}{\partial x_i} + C_D\,\frac{\overline{\rho}\,(2\,k)^{3/2}}{L_d} \\ &+ \frac{\partial}{\partial x_i}\left(\frac{\mu_t}{N_e}\,\frac{\partial \widetilde{e}}{\partial x_i}\right) \,,\end{aligned} \tag{7}$$

$$\begin{aligned}\overline{\rho}\,\frac{Dk}{Dt} =& \overline{\rho}\,\tau_{ij}\,\frac{\partial \widetilde{u}_i}{\partial x_j} + a_i\,\frac{\partial \overline{p}}{\partial x_i} - C_D\,\frac{\overline{\rho}\,(2\,k)^{3/2}}{L_d} \\ &+ \frac{\partial}{\partial x_i}\left(\frac{\mu_t}{N_k}\,\frac{\partial k}{\partial x_i}\right) \,,\end{aligned} \tag{8}$$

$$\begin{aligned}\overline{\rho}\,\frac{DL_t}{Dt} =& C_{L1}\,\overline{\rho}\,\sqrt{2\,k} + C_{L2t}\,\overline{\rho}\,\tau_{ij}\,\frac{L_t}{k}\,\frac{\partial \widetilde{u}_i}{\partial x_j} \\ &+ \frac{\partial}{\partial x_i}\left(\frac{\mu_t}{N_{Lt}}\,\frac{\partial L_t}{\partial x_i}\right) \,,\end{aligned} \tag{9}$$

$$\begin{aligned}\overline{\rho}\,\frac{DL_d}{Dt} =& C_{L1}\,\overline{\rho}\,\sqrt{2\,k} + C_{L2d}\,\overline{\rho}\,\tau_{ij}\,\frac{L_d}{k}\,\frac{\partial \widetilde{u}_i}{\partial x_j} \\ &+ \frac{\partial}{\partial x_i}\left(\frac{\mu_t}{N_{Ld}}\,\frac{\partial L_d}{\partial x_i}\right) \,,\end{aligned} \tag{10}$$

$$\begin{aligned}\overline{\rho}\,\frac{Da_j}{Dt} =& C_B^2\, b\,\frac{\partial \overline{p}}{\partial x_j} - C_a\,\overline{\rho}\,a_j\,\frac{\sqrt{2\,k}}{L_d} + \tau_{ij}\,\frac{\partial \overline{\rho}}{\partial x_i} \\ &+ \frac{\partial}{\partial x_i}\left(\frac{\mu_t}{N_a}\,\frac{\partial a_j}{\partial x_i}\right) \,,\end{aligned} \tag{11}$$

where

$$\frac{D}{Dt} \equiv \frac{\partial}{\partial t} + \widetilde{u}_i\,\frac{\partial}{\partial x_i} \,, \tag{12}$$

$$\mu_t = C_\mu\,\overline{\rho}\,\sqrt{2\,k}\,L_t \,, \tag{13}$$

$$b = \overline{\rho}\,\frac{\sum_\alpha \frac{V_\alpha}{\rho_\alpha}}{\sum_\alpha V_\alpha} - 1 \,, \tag{14}$$

$$\widetilde{S}_{ij} = \frac{1}{2}\left(\frac{\partial \widetilde{u}_i}{\partial x_j} + \frac{\partial \widetilde{u}_j}{\partial x_i}\right) - \frac{1}{3}\,\frac{\partial \widetilde{u}_k}{\partial x_k}\,\delta_{ij} \,, \tag{15}$$

$$\overline{\rho}\,\tau_{ij} = C_{dev}\,2\,\mu_t\,\widetilde{S}_{ij} - \frac{2}{3}\,\overline{\rho}\,k\,\delta_{ij} \,. \tag{16}$$

The k-2L-a model differs from the k-L-a model [56] primarily through the use of separate length scale Eqs. (9) and (10). The turbulent transport length scale L_t is used to define the eddy viscosity in Eq. (13) while the

destruction length scale L_d is used to compute dissipation terms in Eqs. (8) and (11). Additionally, the k-$2L$-a model includes production terms in Eqs. (9) and (10) for shear flow and which were previously neglected in the k-L-a model. The k-$2L$-a model differs from the Schwarzkopf model in that the k-$2L$-a model utilizes algebraic closures for τ_{ij} and b. Other terms, including source terms in the a_i and L equations and the turbulent transport of internal energy, also appear differently in the present model compared to the Schwarzkopf model. However, as discussed in the next Section, it is the setting of model coefficients to satisfy self-similarity constraints, rather than the particular form of the model equations, that enables the k-$2L$-a model to accurately predict RT and KH growth. Similar constraints can be derived for virtually any model that separates turbulent destruction and transport processes by solving two separate transport equations for turbulence length scale L, turbulence dissipation rate ε, or any composite field $Z \equiv C_Z k^m \varepsilon^n$ for some constant C_Z and arbitrary exponents m and n. The present work focuses on the two-length-scale form of the k-L-a model, but a similar approach to self-similarity could be utilized for other Reynolds-averaged models.

III. SIMILARITY ANALYSIS

As done previously for the k-L-a model [56], an ansatz of self-similarity is used to determine values for the model coefficients listed in the previous Section. Self-similarity analysis for buoyancy-driven instability follows very closely that for the k-L-a model and shall only be summarized here. Details of this analysis can be found in Appendix A.

For simplicity of notation in this Section, the overbar to indicate Reynolds-average quantities has been omitted. Assumptions of incompressible flow and, where appropriate, low Atwood number are additionally used.

As discussed in detail in Appendix A, a change of variable is introduced in terms of the mixing layer half-width, $h(t)$, such that $\chi \equiv x/h$. It is then assumed that k, L_t, and L_d are separable in space and time such that $k\,(\chi,t) = K_0(t) f(\chi)$, $L_t\,(\chi,t) = L_{t0}(t)\sqrt{f(\chi)}$, and $L_d\,(\chi,t) = L_{d0}(t)\sqrt{f(\chi)}$ for $f(\chi) = 1-\chi^2$.

A. Constraints from buoyancy-driven instability

It follows from the self-similarity analysis of buoyancy-driven instability that the diffusion coefficients must all be related by

$$N_Y = N_e = N_k = N_a = 2\,N_{Lt} = 2\,N_{Ld}\,. \tag{17}$$

The ratio of the k dissipation coefficient, C_D, to the L production coefficient, C_{L1}, is related through the RM growth exponent, θ, according to

$$\frac{C_D}{C_{L1}} = \frac{2-3\,\theta}{4\,\theta}\,. \tag{18}$$

The decay exponent, n, of homogeneous isotropic turbulence (HIT) is additionally related to this ratio according to [56]

$$n = \frac{2\,C_D}{C_{L1}+C_D} = \frac{2\,C_D/C_{L1}}{1+C_D/C_{L1}}\,. \tag{19}$$

However, the constraints given by Eqs. (18) and (19) are not independent; only one may be used to fix the ratio C_D/C_{L1}, while the other should be checked for consistency.

The buoyancy production coefficient, C_B, is constrained by the RT bubble growth parameter, α_b, according to

$$C_B = \frac{4\,\alpha_b\left(1+2\,\frac{C_D}{C_{L1}}\right)}{\sqrt{\frac{C_\mu\,C_{L1}}{N_k}}}\,. \tag{20}$$

The ratio $C_\mu C_{L1}/N_k$ is constrained by the RT growth parameter and ratio of kinetic energy, E_K, to the change in potential energy, ΔPE, according to

$$\frac{C_\mu\,C_{L1}}{N_k} = 8\,\alpha_b\,\frac{\Delta\mathrm{PE}}{E_K}\,. \tag{21}$$

Finally, the a dissipation coefficient, C_a, is constrained according to

$$C_a = C_D + \frac{\sqrt{\frac{C_{L1}\,N_k}{C_\mu}}}{6\,C_B} - \frac{C_{L1}}{4}\,. \tag{22}$$

B. Analysis for shear-driven instability

Consider the case of a quasi-1D shear layer such that u_x is a linear function of the single spatial dimension, y, and $u_y = 0$. A change of variable is again introduced in terms of the mixing layer half-width such that the similarity variable is $\chi \equiv y/h(t)$. The mean velocity profile is

$$u_x(\chi) = \begin{cases} U_2, & \chi \geq 1 \\ U_1 + \frac{\Delta U}{2}\,(\chi+1)\,, & -1 < \chi < 1 \\ U_1, & \chi \leq -1\,, \end{cases} \tag{23}$$

where $\Delta U = U_2 - U_1$.

1. *Self-similarity of the L_t equation*

For the quasi-1D shear flow described above, Eq. (9) reduces to

$$\begin{aligned}\rho\,\frac{DL_t}{Dt} =& C_{L1}\,\rho\,\sqrt{2\,k} + \frac{L_t}{k}\,C_{L2t}\,\tau_{xy}\,\frac{\partial u_x}{\partial y} \\ &+ \frac{\partial}{\partial y}\left(\frac{\mu_t}{N_{Lt}}\,\frac{\partial L_t}{\partial y}\right)\,,\end{aligned} \tag{24}$$

where

$$\tau_{xy} = C_{dev}\,\mu_t\,\frac{\partial u_x}{\partial y}\,. \tag{25}$$

After applying the assumption of incompressibility and substituting, Eq. (24) becomes

$$\begin{aligned}\frac{D}{Dt}\left(L_{t0}f^{1/2}\right) &= C_{L1}\sqrt{2K_0}f^{1/2} \\ &+ \frac{L_{t0}}{K_0}f^{-1/2}\left[C_{L2t}C_{dev}C_\mu L_{t0}f\sqrt{2K_0}\left(\frac{\partial u_x}{\partial y}\right)^2\right] \\ &+ \frac{\partial}{\partial y}\left[\frac{C_\mu L_{t0}f\sqrt{2K_0}}{N_{Lt}}\frac{\partial}{\partial y}\left(L_{t0}f^{1/2}\right)\right]\,. \end{aligned}\tag{26}$$

Assuming that the transport length scale grows self-similarly according to $L_{t0}(t) = \beta h(t)$, Eq. (26) is further transformed to

$$\begin{aligned}\dot{L}_{t0} &= \sqrt{2K_0}\left[C_{L1} + \frac{\beta^2 C_{L2t}C_{dev}C_\mu}{4}\frac{(\Delta U)^2}{K_0} - \frac{C_\mu}{N_{Lt}}\beta^2\right] \\ &- \sqrt{2K_0}\left[C_{L1} + \frac{\beta^2 C_{L2t}C_{dev}C_\mu}{4}\frac{(\Delta U)^2}{K_0} - \frac{2C_\mu}{N_{Lt}}\beta^2\right]\chi^2\,, \end{aligned}\tag{27}$$

where a dot indicates differentiation with respect to time. In order to satisfy the self-similarity ansatz, it is necessary that the right-hand-side terms proportional to χ^2 vanish, i.e., if

$$\beta^2 = \frac{4\,C_{L1}\,N_{Lt}}{C_\mu\,(8 - N_{Lt}\,C_{L2t}\,C_{dev}\Phi)}\,, \tag{28}$$

where the turbulence intensity is

$$\Phi^{-1} \equiv \frac{K_0}{(\Delta U)^2}\,. \tag{29}$$

For a free shear layer, Φ is expected to be a constant [18]. Substituting Eq. (28) into Eq. (27) reduces the L_t transport equation to

$$\dot{L}_{t0} = C_{L1}\left(1 - \frac{4 - N_{Lt}\,C_{L2t}\,C_{dev}\,\Phi}{8 - N_{Lt}\,C_{L2t}\,C_{dev}\,\Phi}\right)\sqrt{2\,K_0}\,. \tag{30}$$

2. *Self-similarity of the L_d equation*

For quasi-1D shear flow, Eq. (10) reduces to

$$\begin{aligned}\rho\,\frac{DL_d}{Dt} =& C_{L1}\,\rho\,\sqrt{2\,k} + \frac{L_d}{k}\,C_{L2d}\,\tau_{xy}\,\frac{\partial u_x}{\partial y} \\ &+ \frac{\partial}{\partial y}\left(\frac{\mu_t}{N_{Ld}}\,\frac{\partial L_d}{\partial y}\right)\,. \end{aligned}\tag{31}$$

Utilizing the incompressibility assumption and substituting into Eq. (31) gives

$$\begin{aligned}\left(\dot{L}_{t0}\frac{L_{d0}}{L_{t0}} - \dot{L}_{d0}\right)\chi^2 + \dot{L}_{d0} &= C_{L1}\sqrt{2K_0}\left(1-\chi^2\right) \\ &+ \frac{\beta^2 C_{L2d}C_{dev}C_\mu}{4}\sqrt{2K_0}\Phi\frac{L_{d0}}{L_{t0}}\left(1-\chi^2\right) \\ &+ \frac{C_\mu}{N_{Ld}}\beta^2\sqrt{2K_0}\frac{L_{d0}}{L_{t0}}\left(2\chi^2-1\right)\,. \end{aligned}\tag{32}$$

Collecting terms, rearranging, and substituting Eq. (30) gives

$$\dot{L}_{d0} = \sqrt{2K_0}\left(C_{L1} + \frac{\beta^2 C_{L2d}C_{dev}C_\mu\Phi}{4}\frac{L_{d0}}{L_{t0}} - \frac{C_\mu}{N_{Ld}}\beta^2\frac{L_{d0}}{L_{t0}}\right)\,, \tag{33}$$

and

$$\begin{aligned}\dot{L}_{d0} &= \sqrt{2K_0}\left(C_{L1} + \frac{\beta^2 C_{L2d}C_{dev}C_\mu\Phi}{4}\frac{L_{d0}}{L_{t0}} - \frac{2C_\mu}{N_{Ld}}\beta^2\frac{L_{d0}}{L_{t0}}\right) \\ &+ C_{L1}\left(1 - \frac{4 - N_{Lt}C_{L2t}C_{dev}\Phi}{8 - N_{Lt}C_{L2t}C_{dev}\Phi}\sqrt{2K_0}\right)\frac{L_{d0}}{L_{t0}}\,, \end{aligned}\tag{34}$$

which must be satisfied simultaneously. It follows that $N_{Lt} = N_{Ld}$. Applying this constraint to Eq. (34) reduces it to Eq. (33). After further algebraic manipulation to eliminate the spatial dependence, the relationship

$$\frac{L_{d0}}{L_{t0}} = \frac{8 - N_{Lt}\,C_{L2t}\,C_{dev}\,\Phi}{8 - N_{Ld}\,C_{L2d}\,C_{dev}\,\Phi} \tag{35}$$

must be satisfied.

An implication of Eq. (35) is that the self-similarity ansatz requires the ratio between the two length scales to be constant for canonical KH instability. However, in the general case, Φ is not necessarily constant and neither will be the ratio L_{d0}/L_{t0}. The behavior of L_{d0}/L_{t0} under combined instability conditions will be investigated in Section IV. Here, only the case of a canonical KH mixing layer is considered. Substituting Eq. (35) into Eq. (32) gives

$$\dot{L}_{d0} = C_{L1}\left(1 - \frac{4 - N_{Lt}\,C_{L2t}\,C_{dev}\,\Phi}{8 - N_{Ld}\,C_{L2d}\,C_{dev}\,\Phi}\right)\sqrt{2\,K_0}\,. \tag{36}$$

3. *Self-similarity of the mean momentum equation*

For the incompressible shear layer described by Eq. (23) with no body force, Eq. (6) reduces to

$$\frac{Du_x}{Dt} = \frac{\partial \tau_{xy}}{\partial y}\,. \tag{37}$$

After evaluating derivatives and substituting, Eq. (37) reduces to

$$\dot{h} = 2\,C_{dev}\,C_\mu\,\beta\,\sqrt{2\,K_0}\,. \tag{38}$$

Utilizing Eq. (30) to substitute for $\sqrt{2K_0}$ reduces Eq. (38) to the constraint

$$C_{dev} = \frac{1}{2\,N_{Lt}}\,. \tag{39}$$

4. Self-similarity of the k equation

For quasi-1D shear flow, Eq. (8) reduces to

$$\rho \frac{Dk}{Dt} = \frac{\partial}{\partial y}\left(\frac{\mu_t}{N_k}\frac{\partial k}{\partial y}\right) - \rho C_D \frac{(2k)^{3/2}}{L_d} + \tau_{xy}\frac{\partial u_x}{\partial y}\,. \quad (40)$$

Substituting and utilizing the incompressibility assumption to drop factors of ρ leads to

$$\begin{aligned}\frac{D}{Dt}(K_0 f) = \frac{\partial}{\partial y}\left[\frac{C_\mu L_{t0} f\sqrt{2K_0}}{N_k}\frac{\partial}{\partial y}(K_0 f)\right] \\ - C_D\frac{(2K_0)^{3/2}}{L_{d0}}f \\ + C_{dev}C_\mu L_{t0}\sqrt{2K_0}\left(\frac{\Delta U^2}{4h^2}\right)f\,. \end{aligned} \quad (41)$$

As Φ is expected to be constant, $\dot{K}_0 = 0$ for free shear flow. Then, after expanding derivatives, collecting terms, and utilizing Eq. (39), Eq. (41) reduces to

$$\left[\frac{C_\mu}{N_k}\beta^2 + C_D\frac{L_{t0}}{L_{d0}} - \frac{C_{dev}C_\mu\Phi}{8}\beta^2\right] - \left[\frac{3C_\mu}{N_k}\beta^2 - C_{L1}\left(1 - \frac{8 - C_{L2t}\Phi}{16 - C_{L2t}\Phi}\right) + C_D\frac{L_{t0}}{L_{d0}} - \frac{C_{dev}C_\mu\Phi}{8}\beta^2\right]\chi^2 = 0\,. \quad (42)$$

This equation is satisfied if

$$C_{L1}\left(1 - \frac{8 - C_{L2t}\,\Phi}{16 - C_{L2t}\,\Phi}\right) = \frac{16}{N_k}\frac{C_{L1}\,N_{Lt}}{16 - C_{L2t}\,\Phi}\,, \quad (43)$$

which requires the constraint $N_k = 2N_{Lt}$. Substituting this constraint into Eq. (42) gives a single expression, which can be rearranged to obtain

$$C_{L2d} = 4\left(4 + \frac{C_{L1}}{C_D}\right)\Phi^{-1} - \frac{C_{L1}}{2\,C_D}\,. \quad (44)$$

Equivalently, Eq. (44) can be rearranged to solve for the steady-state turbulence intensity

$$\Phi^{-1} = \frac{2\,C_{L2d}\,C_D + C_{L1}}{8\,(4\,C_D + C_{L1})}\,, \quad (45)$$

which is a function of C_{L2d} but not of C_{L2t}. Additionally, if the ratio C_D/C_{L1} is fixed by the RM growth exponent according to Eq. (18), then C_{L2d} is the only free model coefficient in Eq. (45).

5. Kelvin–Helmholtz growth parameter

For a spatially evolving shear layer, the nondimensional growth parameter, δ, is defined as

$$\delta \equiv \frac{dh}{dx}\,. \quad (46)$$

Thus, for a temporally evolving shear layer,

$$\dot{h} = \frac{dh}{dx}\frac{dx}{dt} = \delta\,U_c\,, \quad (47)$$

where $U_c \equiv (U_1 + U_2)/2$ is the convective velocity [58]. Recognizing that $\dot{h} = \dot{L}_{t0}/\beta$, Eq. (30) is used to derive the constraint

$$C_{L2t} = 16\,\Phi^{-1} - 128\,\Phi^{-2}\,\frac{C_{L1}\,C_\mu}{N_k}\left(\frac{\mathcal{A}}{\delta}\right)^2\,, \quad (48)$$

where

$$\mathcal{A} \equiv \frac{U_2 - U_1}{U_2 + U_1} \quad (49)$$

is the shear analogue of the Atwood number. Equivalently, Eq. (48) can be rearranged to solve for

$$\frac{\delta}{\mathcal{A}} = 8\sqrt{\frac{2\,C_{L1}\,C_\mu}{N_k\,(16 - C_{L2t}\,\Phi)}\,\Phi^{-1}}\,, \quad (50)$$

which implies $C_{L2t} < 16\Phi^{-1}$ for this quantity to be real-valued.

As Eq. (50) illustrates, the expected growth parameter is a function of C_{L2t} but not of C_{L2d}. Moreover, if the ratio $C_{L1}C_\mu/N_k$ is fixed by RT self-similarity constraints according to Eq. (21), then C_{L2t} is the only free model coefficient in Eq. (50). This highlights the main benefit of a two-length-scale model over a single-length-scale model. In a single-length-scale model, $C_{L2t} = C_{L2d}$, and *it is not possible to decouple the turbulence intensity from the growth rate for a quasi-1D shear layer.* However, as demonstrated by Eqs. (45) and (50), the two-length-scale model allows one to choose model coefficients that can independently set the turbulence intensity and growth parameter of a free shear layer.

TABLE I. Summary of model coefficients and the experimental values that constrain them.

α_b	$\frac{E_K}{\Delta \mathrm{PE}}$	θ	Φ^{-1}	$\frac{\delta}{\mathcal{A}}$	C_μ	C_a	C_B	C_D	C_{dev}	C_{L1}	C_{L2d}	C_{L2t}	N_a	N_e	N_k	N_{Ld}	N_{Lt}	N_Y
0.06	0.50	0.25	0.035	0.08	0.204	0.339	0.857	0.354	16.67	0.283	0.272	-22.96	0.060	0.060	0.060	0.030	0.030	0.060

C. Summary of constraints

Equations (17), (18), (20)–(22), (39), (44), and (48) provide 12 constraints on 14 model coefficients. Note that C_μ and C_D may be regarded as scaling coefficients on the turbulence transport and destruction length scales, respectively. Therefore, these values are chosen here to be consistent with the k-L-a model [56] such that $C_\mu\sqrt{2} = 0.288$ and $C_D 2^{3/2} = 1$. The same set of experimental values as for the k-L-a model are used to set the RT growth parameter $\alpha_b = 0.06$ [21, 59], the RT energetics ratio $E_K/\Delta PE = 0.5$ [23, 59], and the RM growth exponent $\theta = 0.25$ [21, 60]. This choice of θ results in an HIT decay exponent $n \approx 1.11$. Additionally, the KH turbulence intensity $\Phi^{-1} = 0.035$ and growth parameter $\delta/\mathcal{A} = 0.08$ are set according to free shear layer experimental measurements by Bell and Mehta [18, 29].

Table I summarizes the complete set of model coefficients as well as the experimental values used to constrain them. For this choice of model coefficients, $C_{L2t} < 0$ while $C_{L2d} > 0$. This follows directly from the self-similarity analysis; as illustrated by Eq. (50), a negative value of C_{L2t} guarantees a real-valued KH growth parameter. If, instead, $C_{L2t} = C_{L2d}$ (as is the case in a single-length-scale model) then for the choice of experimental values, Eq. (50) predicts $\delta/\mathcal{A} \approx 0.72$, which is approximately nine times greater than desired.

The similarity analysis presented in this Section has relied upon assumptions of incompressibility and low Atwood number. Therefore, it may be expected that model accuracy should degrade for higher Mach and Atwood number flows. The k-L-a model, however, has been previously demonstrated to give reasonable agreement with experiment in shocked flows up to Mach 1.98 at Atwood numbers up to 0.67 [56]. Since the k-2L-a model reduces to the single-length-scale model for flows without shear, it is expected that the two-length-scale model should be similarly valid in applications to moderately compressible mixing layers. No assumptions have been made in the similarity analysis regarding the strength of shearing. As discussed in more detail in Section IV, while stress limiting may be beneficial for numerical stability in simulations with strong shearing, there is no apparent analytical reason why the model should not be valid for arbitrarily strong or weak shearing.

In the next Section, the two-length-scale model is applied to one-dimensional simulations of RT, RM, KH, and combined RT/KH instability. It will be shown that when model coefficients are set according to the self-similarity constraints derived in this Section, the anticipated growth parameters are recovered.

IV. NUMERICAL RESULTS

The k-2L-a model is applied here to the simulation of several one-dimensional RT, RM, KH, and combined RT/KH test problems. The model is implemented in the ARES code, which is a second-order arbitrary Lagrangian/Eulerian (ALE) hydrodynamics code developed at Lawrence Livermore National Laboratory (LLNL) [61]. Simulations of buoyancy-driven instability are considered first to confirm that the k-2L-a model is able to reproduce the same level of agreement previously demonstrated for the k-L-a model. Simulations of shear-driven KH instability and combined RT/KH instability are then performed to confirm that the k-2L-a model is able to simultaneously match the expected turbulence intensity and growth parameter.

A. Rayleigh–Taylor mixing

First consider a one-dimensional hydrostatic RT mixing layer between two ideal, monatomic gases subject to constant acceleration at Atwood number, $A = 0.05$. This problem is set up in a domain of size 1 cm with 1600 uniformly spaced computational zones. Turbulence length scales are initialized to zero everywhere except for the two zones bordering the interface at $y = 0$, where $L_d = L_t = \lambda_0 = 4.0 \times 10^{-6}$ cm. Turbulence kinetic energy is initialized to zero everywhere except the two interface zones, where k is initialized to 1.0 cm^2/s^2.

In Fig. 1 (a), the mixing layer width, the turbulence kinetic energy, and the turbulence length scales are plotted for simulations using the k-L-a and the k-2L-a models. By plotting these quantities against Agt^2, they increase linearly, which implies a quadratic growth αAgt^2. The results from the k-2L-a model follow the results of the k-L-a model exactly. Additionally, in the k-2L-a model, the transport length scale is equal to the destruction length scale; this agrees with the relationship predicted by Eq. (A9). Figure 1 (b) illustrates that for both the k-L-a and k-2L-a models, the realized growth parameter α_b asymptotes to the expected value 0.06, which was used to set the model coefficients.

Figure 2 shows the normalized profiles of species mass fraction (Y_H), turbulence kinetic energy (k), mass-flux velocity (a_y), and density–specific-volume covariance (b) obtained from the k-L-a and k-2L-a models. These re-

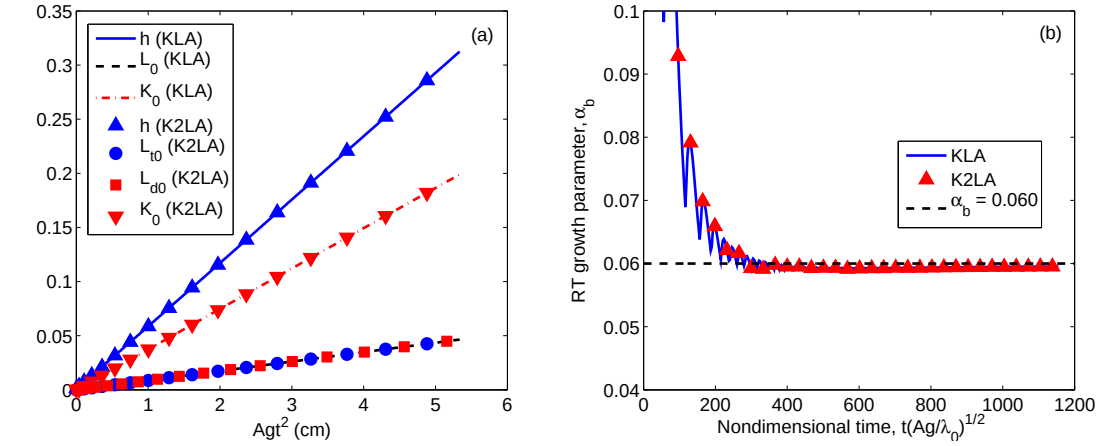

FIG. 1. Mixing layer growth in a one-dimensional RT mixing layer. (a) Mixing layer half-width, turbulence kinetic energy, and turbulence length scales are plotted as a function of time squared for both the k-L-a and k-2L-a models. (b) The RT growth parameter, $\alpha_b = h/\left(Agt^2\right)$, is plotted as a function of nondimensional time for both the k-L-a and k-2L-a models.

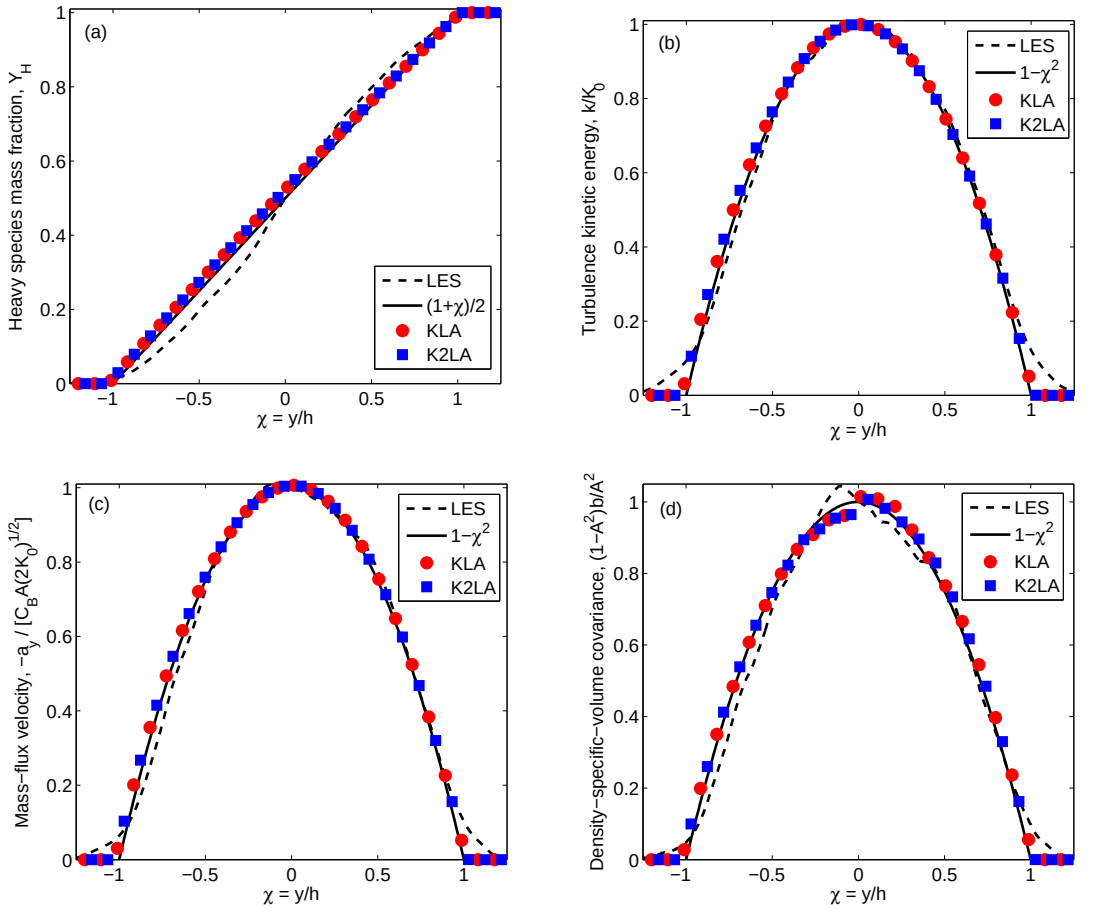

FIG. 2. Normalized self-similar profiles in a one-dimensional RT mixing layer at $A = 0.05$: (a) heavy species mass fraction Y_H, (b) turbulence kinetic energy k, (c) mass-flux velocity a_y, and (d) density–specific-volume covariance b profiles, for the k-L-a and k-2L-a models compared with LES results [48].

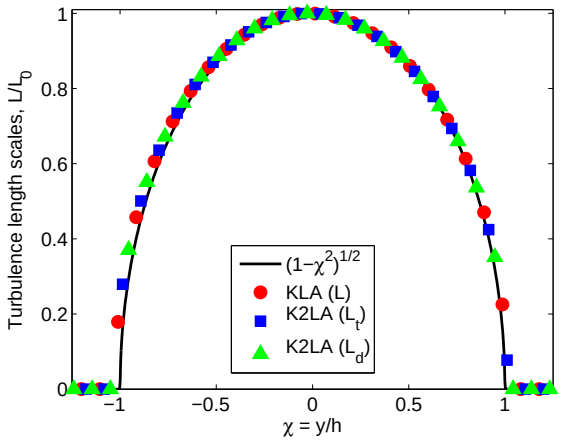

FIG. 3. Normalized self-similar profiles of turbulence length scales in a one-dimensional RT mixing layer are compared between the k-L-a and k-$2L$-a models.

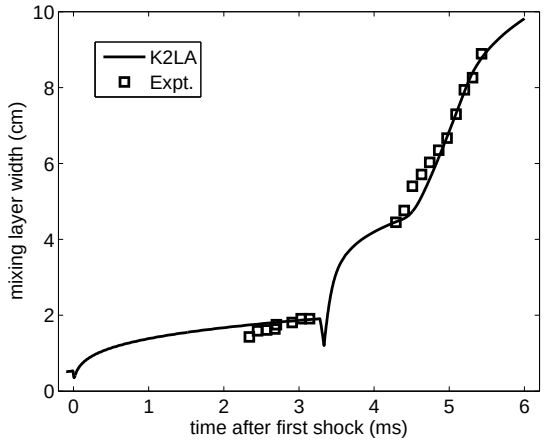

FIG. 4. Mixing width as a function of time for the Vetter and Sturtevant shock tube experiment [19]. Symbols indicate experimental data, while the solid line indicates simulation results with the k-$2L$-a model.

sults are compared against the expected self-similar profiles as well as results from LES [48]. It is evident that the k-$2L$-a results agree quite closely with the expected self-similar profiles and with the k-L-a model. These profiles are also in reasonably close agreement with the LES data.

Figure 3 compares the self-similar profiles of turbulence length scales obtained with the k-L-a and k-$2L$-a models. Again, the two models agree well with each other and with the expected self-similar profile. Indeed, $L_d/L_t = 1$ across the entire mixing layer in the k-$2L$-a model, in accordance with the earlier observation in Fig. 1 and with the results of the similarity analysis in Appendix A. For a pure RT mixing layer, there is no difference between the results of the k-L-a and the k-$2L$-a models.

B. Richtmyer–Meshkov mixing

The k-$2L$-a model is next applied to simulation of the Mach 1.5 air/SF_6 shock tube experiment ($A \approx 0.67$) by Vetter and Sturtevant [19]. The shockwave is driven from air into SF_6, is reflected from the endwall, and eventually shocks the fluid interface for a second time (usually referred to as *reshock*). In this particular experiment, a rarefaction wave additionally interacts with the mixing layer shortly after the second shock.

Simulation results are found to be well converged with 2560 zones in the 60.0 cm SF_6 test section, 3840 zones of shocked air (157 cm), and 80 zones of ambient air (6.0 cm). An initially diffuse interface of width $h_0 = 0.11$ cm is assumed, and the initial conditions are

$$\begin{aligned} Y_{SF_6}(y,0) &= \frac{1}{2}\left[1+\tanh\left(\frac{y}{h_0}\right)\right], \\ L_d(y,0) = L_t(y,0) &= 4\,\lambda_0\,Y_{SF_6}(y)\,[1-Y_{SF_6}(y)] \\ k(y,0) &= 4\,k_0\,Y_{SF_6}(y)\,[1-Y_{SF_6}(y)]\ . \end{aligned} \quad (51)$$

The initial length scales and turbulence kinetic energy are initialized with a smooth profile, where $\lambda_0 = 0.0225$ cm and $k_0 = 1.0\times10^{-6}$ cm$^2/\mu$s^2.

As illustrated in Fig. 4, the mixing layer width (defined as the distance between the 1% and 99% Y_{SF_6} contours) compares quite favorably with experiment. The decrease of the mixing width around 3.3 ms corresponds to compression from the reflected shock, while the inflection around 4.5 ms corresponds to interaction of the mixing layer with the rarefaction wave. Such features are observed in both LES [46, 62, 63] as well as RANS simulations [29, 57, 64, 65] of reshocked RM mixing layers. Morgan and Wickett previously demonstrated a similar level of agreement between simulation and experiment for the k-L-a model [56]. As expected, the k-$2L$-a model performs comparably to the k-L-a model in simulations of pure buoyancy-driven RT and RM instability.

In the next Section, the k-$2L$-a model is applied to simulations of shear-driven instability for which it demonstrates an improvement over the k-L-a model.

C. Kelvin–Helmholtz mixing

To illustrate the ability of the k-$2L$-a model to more accurately simulate the evolution of KH mixing layers, the predictions of the k-L-a model and k-$2L$-a model are compared in quasi-1D simulations of the KH mixing layer investigated experimentally by Bell and Mehta [18]. These simulations are run with 960 uniformly-spaced computational zones on a domain extending from $y = -48.0$ cm to $y = 48.0$ cm. Turbulence length scales are initialized to zero everywhere except for the two zones bordering the interface at $y = 0$, where $L_d = L_t = \lambda_0 = 0.44$ cm. Turbulence kinetic energy is additionally initialized to zero everywhere except for the two interface

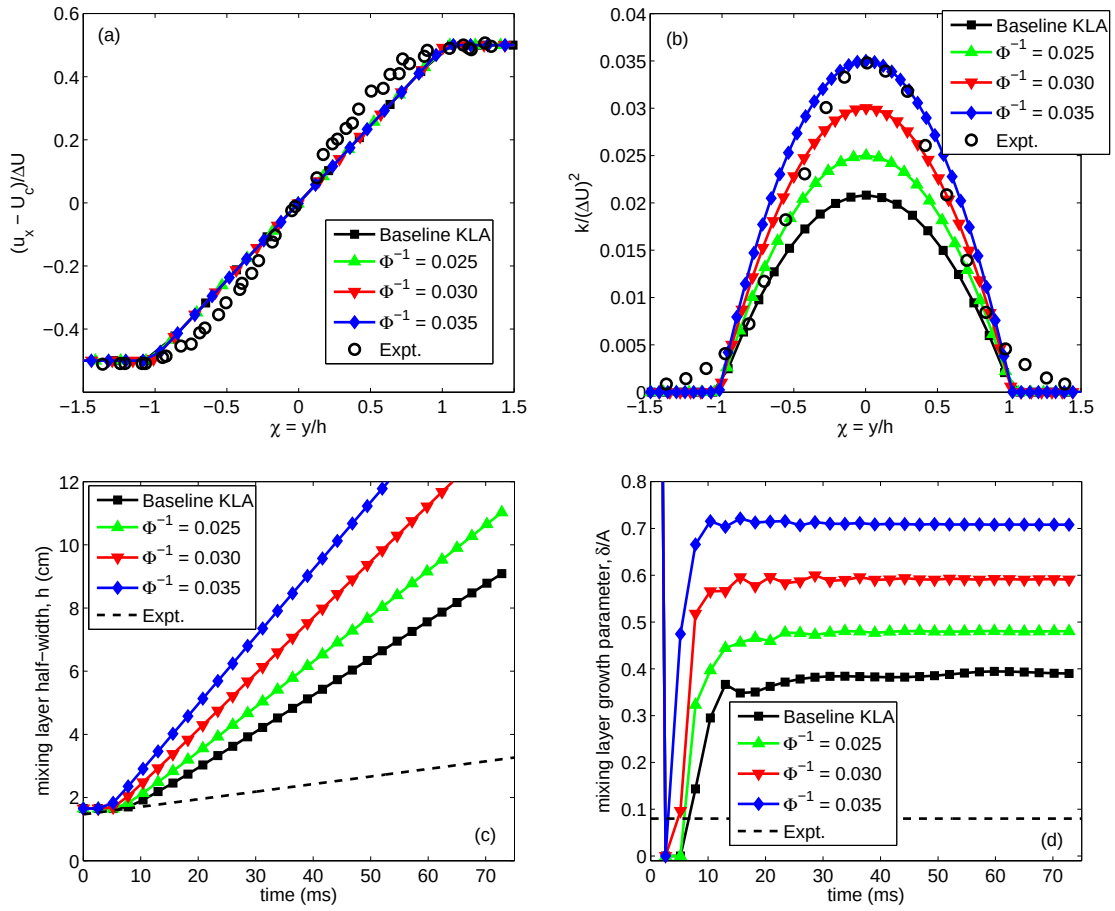

FIG. 5. Self-similar profiles and mixing layer evolution of a KH shear layer simulated with the k-L-a model for several choices of Φ^{-1}: (a) self-similar velocity profile, (b) steady-state turbulence kinetic energy profile, (c) mixing layer half-width as a function of time, and (d) mixing layer growth parameter as a function of time. For all k-L-a results, $C_{L2t} = C_{L2d}$, where C_{L2d} is determined by Eq. (44) except for the *Baseline KLA* results, in which $C_{L2t} = C_{L2d} = 0.0$. Experimental data is taken from Bell and Mehta [18].

zones, where k is initialized to $0.01\,(\Delta U)^2$. The initial velocity profile is chosen to match the Bell and Mehta experiment [18] such that $u_x = U_1 = 900$ cm/s for $y < 0$ and $u_x = U_2 = 1500$ cm/s for $y \geq 0$, corresponding to $\mathcal{A} = 0.25$.

Figure 5 plots self-similar profiles and mixing layer growth parameters obtained from simulations using the single-length-scale k-L-a model. The *Baseline KLA* results illustrate the evolution of the mixing layer predicted when $C_{L2t} = C_{L2d} = 0$. In this case, the peak turbulence intensity [Fig. 5(b)] is significantly under-predicted with respect to experiment, while the mixing layer growth parameter is over-predicted [Fig. 5(d)]. By including the L/k term in the L equation, an additional degree-of-freedom is obtained, and it becomes possible to calibrate the model to reproduce a desired turbulence intensity, Φ^{-1}, as described by Eq. (44). Figure 5(b) illustrates that when C_{L2d} is chosen to satisfy Eq. (44), the maximum value of $k/(\Delta U)^2$ matches the expected Φ^{-1}. However, as Fig. 5(d) illustrates, as the single-length-scale model requires $C_{L2t} = C_{L2d}$, it is not possible with this model to change the turbulence intensity without simultaneously increasing the mixing layer growth parameter; this is the conclusion reached earlier with Eq. (50). As the turbulence intensity is increased to better match the experimental value, discrepancy in the mixing layer growth parameter increases commensurately.

Figure 6 illustrates the principal improvement of the two-length-scale k-2L-a model over the single-length-scale k-L-a model. In this figure (to be compared directly with Fig. 5), self-similar profiles and mixing layer growth parameters are obtained for a number of simulations using the k-2L-a model. For each of the simulations, the turbulence intensity Φ^{-1} is fixed at 0.035, and C_{L2t} is varied independently from C_{L2d} according to Eq. (48) to reproduce a desired mixing layer growth parameter. As Fig. 6(b) illustrates, the expected turbulence intensity is recovered for each case, allowing for calibration to experiment. The degree-of-freedom added by the decoupling of turbulence destruction and transport length scales allows

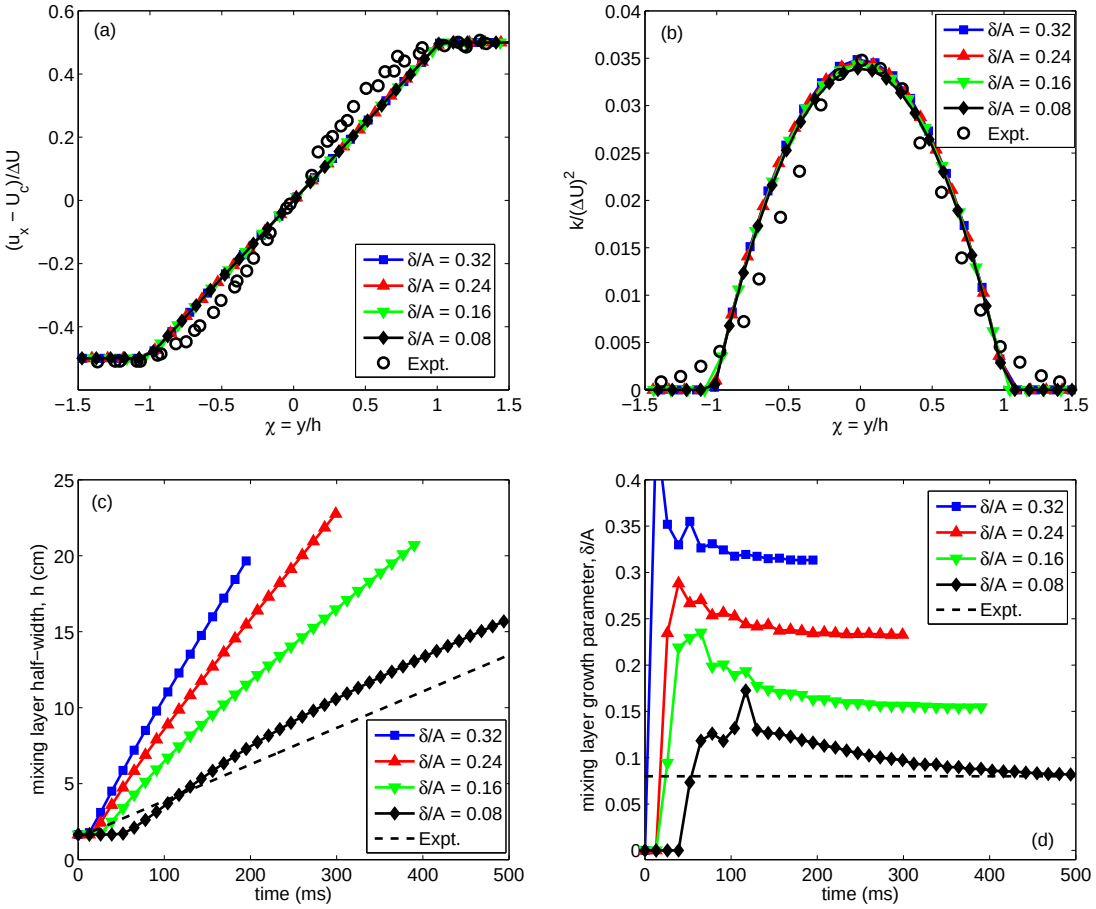

FIG. 6. Self-similar profiles and mixing layer evolution of a KH shear layer simulated with the k-$2L$-a model for several choices of $\delta/\mathcal{A}$: (a) self-similar velocity profile, (b) steady-state turbulence kinetic energy profile, (c) mixing layer half-width as a function of time, and (d) mixing layer growth parameter as a function of time. For all k-$2L$-a results, $\Phi^{-1} = 0.035$, and C_{L2t} is determined by Eq. (48). Experimental data is taken from Bell and Mehta [18].

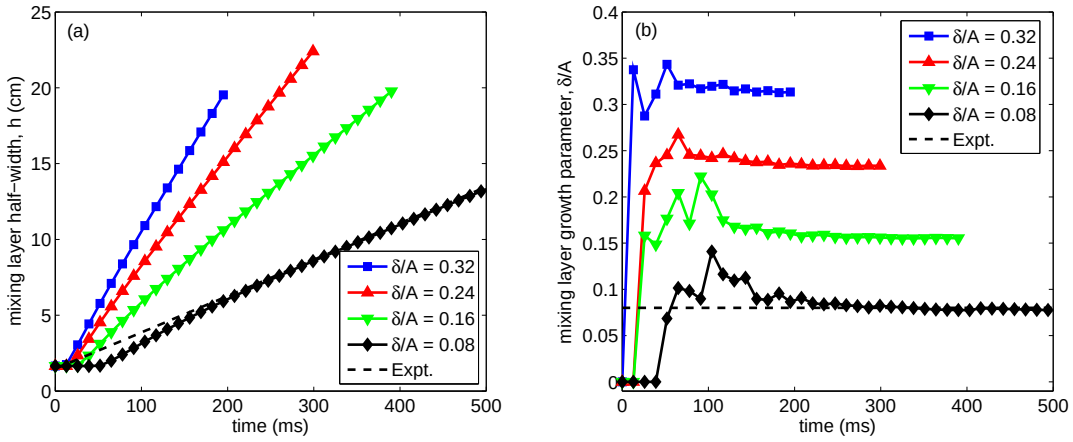

FIG. 7. KH mixing layer half-width and growth parameter for several choices of $\delta/\mathcal{A}$ simulated using the k-$2L$-a model with the stress-limiter modification described in Appendix B. For all simulation results, $\Phi^{-1} = 0.035$, and C_{L2t} is determined by Eq. (48). Experimental growth rate is taken from Bell and Mehta [18].

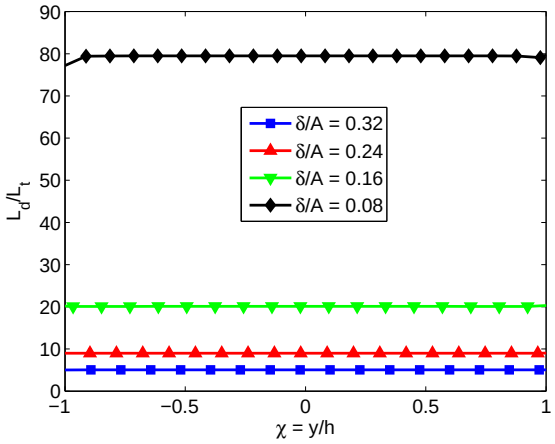

FIG. 8. The ratio of length scales L_d/L_t across a KH shear layer is plotted for several choices of $\delta/\mathcal{A}$. For each case, $\Phi^{-1} = 0.035$ and C_{L2t} is determined by Eq. (48).

for the independent calibration of the growth parameter. As illustrated in Fig. 6(d), after an initial transient period, the k-2L-a model recovers the expected growth parameter for each choice of $\delta/\mathcal{A}$; agreement is obtained with experiment for $\delta/\mathcal{A} = 0.08$. Appendix B describes a stress-limiter modification to the k-2L-a model that may be used to constrain the turbulence time scales, $L_t/\sqrt{2k}$ and $L_d/\sqrt{2k}$, according to realizability conditions in a manner similar to the approach by Durbin [66]. Figure 7 illustrates that when such an approach is applied in simulation of the KH mixing layers under consideration, both the amplitude of growth rate overshoot and the duration of the transient period are reduced.

For each of the cases illustrated in Fig. 6, the ratio of the turbulence length scales across the mixing layer is plotted in Fig. 8. As predicted by Eq. (35), for each case the ratio L_d/L_t is constant across the mixing layer. In contrast to the unity ratio obtained across an RT mixing layer, the ratio across a KH mixing layer is greater than one for each of the cases considered; this should be the case whenever $C_{L2t} < 0$ and $C_{L2d} > 0$. In this regard, the results of Fig. 8 can be quite surprising if one incorrectly assumes L_d to be representative of the dissipative Kolmogorov length scale. In fact, $L_d \propto k^{3/2}/\varepsilon$, which generally is representative of energy-containing length scales. (This potential confusion is why L_d is referred to as the *destruction* length scale in the present work, rather than the *dissipation* length scale.) It can therefore be difficult to ascribe physical significance to the difference between L_d and L_t. Nevertheless, the utility of the two-length-scale model is that it provides a mechanism for separating two length scales that are present among a continuum of scales in fully-developed turbulent mixing layers.

Although the similarity analysis presented in the previous Section relied on an assumption of low Atwood number, in order to probe the limits of model applicability, the k-2L-a model is now applied to the simulation of a variable-density KH mixing layer. In this case, in addition to having different velocities, the two fluid streams are also identified as separate fluid species with different densities. Density ratios $\rho_1/\rho_2 = 1/7$, 1, and 7 are considered, which correspond to similar mixing layers investigated experimentally by Brown and Roshko [17]. Although these simulations are computed without the effect of gravitational acceleration, these density ratios correspond to Atwood numbers 0.75, 0.0, and -0.75, respectively. The velocity ratio is set at $U_1/U_2 = 1/\sqrt{7}$, which corresponds to $\mathcal{A} \approx 0.45$.

Results of the variable-density KH mixing layer simulations are illustrated in Fig. 9. For each of the simulations, model coefficients are set according to the values in Table I, for an expected $\Phi^{-1} = 0.035$ and $\delta/\mathcal{A} = 0.08$. A significant Atwood number effect is apparent in the skewed mass fraction and turbulence kinetic energy profiles. Similar skewed profiles were previously observed for moderate-to-large Atwood number RT mixing layers [56]. Additionally, $k/(\Delta U)^2$ peaks roughly 14% higher than expected, and the mixing layer growth parameter reaches a value about 10% lower than expected for both of the variable density cases. In the experimental work by Brown and Roshko [17], growth parameters of approximately 0.054, 0.081, and 0.095 were reported for the $\rho_1/\rho_2 = 7$, 1, and 1/7 cases, respectively.

Although the k-2L-a model does predict some impact on the growth parameter due to variable density effects, the predicted impact is not as significant as the variations reported by Brown and Roshko, and the effect is the same for both the $A = 0.75$ and -0.75 cases. In the absence of gravity, there is no apparent mechanism in the model equations that could capture such an asymmetric effect as reported by Brown and Roshko. It is therefore uncertain if the variable-density impact on KH growth rate observed by Brown and Roshko is a physical process not accounted for by the k-2L-a model or if it might be the result of some gravitational effect or transient behavior present in the experimental system that is not present in the current simulations. Further research, likely to include high-fidelity simulation of variable-density KH mixing, would be necessary to answer this question. For the present purposes, the results of Fig. 9 demonstrate that the k-2L-a model may be applied to the simulation of high-Atwood-number, variable-density KH mixing with little departure from the anticipated level of turbulence intensity and mixing layer growth parameter.

D. Combined Rayleigh–Taylor/Kelvin–Helmholtz mixing

The k-2L-a model, with model coefficients given in Table I, is now applied to the simulation of combined RT/KH instability. In the case of combined RT/KH instability, the relative strength of buoyancy to shear effects

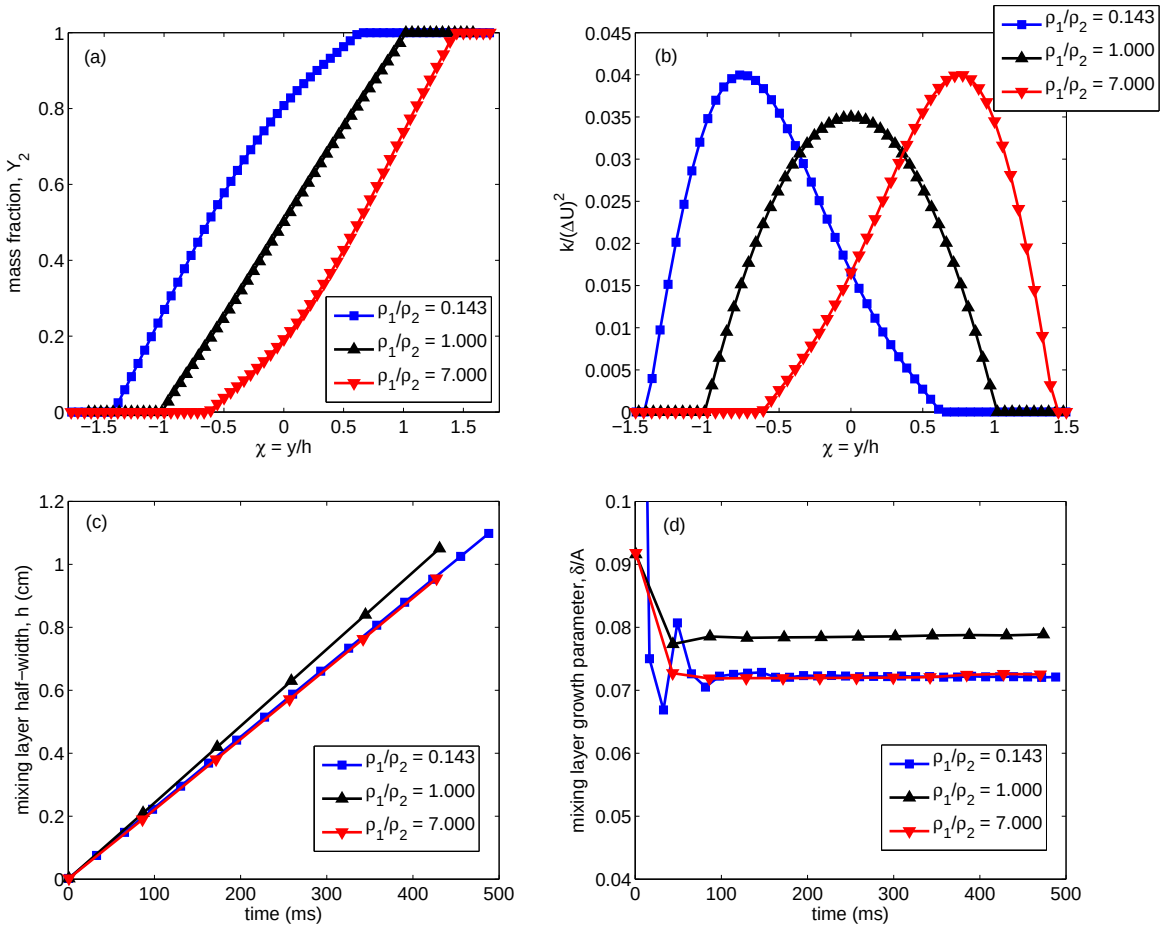

FIG. 9. Self-similar profiles and mixing layer evolution of variable-density KH shear layers simulated with the k-2L-a model for several choices of ρ_1/ρ_2: (a) self-similar velocity profile, (b) steady-state turbulence kinetic energy profile, (d) mixing layer half-width as a function of time, and (d) mixing layer growth parameter as a function of time. For all cases, the expected values are $\Phi^{-1} = 0.035$ and $\delta/\mathcal{A} = 0.08$.

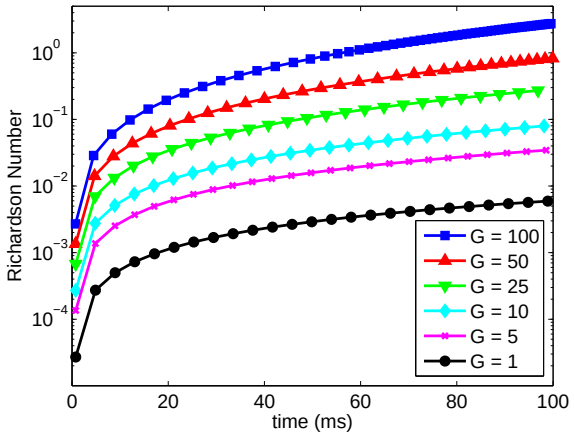

FIG. 10. Richardson number as a function of time for several k-2L-a simulations of a combined RT/KH mixing layer with varying levels of gravitational acceleration. Acceleration is indicated in terms of a multiplier on Earth gravity such that $g = Gg_e$.

is given by the Richardson number [52]

$$\mathrm{Ri} = -\frac{g\,\partial\overline{\rho}/\partial y}{(\partial\tilde{u}/\partial y)^2} \approx -\frac{2\,g\,A\,h}{(\Delta U)^2}\,. \tag{52}$$

To investigate model behavior across a range of Richardson numbers, a quasi-1D mixing layer is simulated at $A = 0.05$ and $\mathcal{A} = 0.5$ for varying intensity of gravitational acceleration. Figure 10 illustrates the Richardson number time-evolution for simulations with acceleration $g = Gg_e$ for a constant multiplier G on Earth gravity, g_e (980.7 cm/s^2). For these simulations, several decades are explored ranging between $\mathrm{Ri} \approx 2 \times 10^{-5}$ and 3. These simulations allow an exploration of behavior ranging between KH- and RT-dominated instability.

As discussed previously, in the low-Atwood-number limit the half-width of a self-similar RT mixing layer is expected to grow according to $h = \alpha_b A g t^2$. Similarly, the half-width of a self-similar KH mixing layer is expected to grow according to Eq. (47), $h = \delta U_c t = (\delta/\mathcal{A})\,(\Delta U/2)\,t$. If the combined RT/KH mixing layer width is a linear combination of the expected RT and KH mixing layer

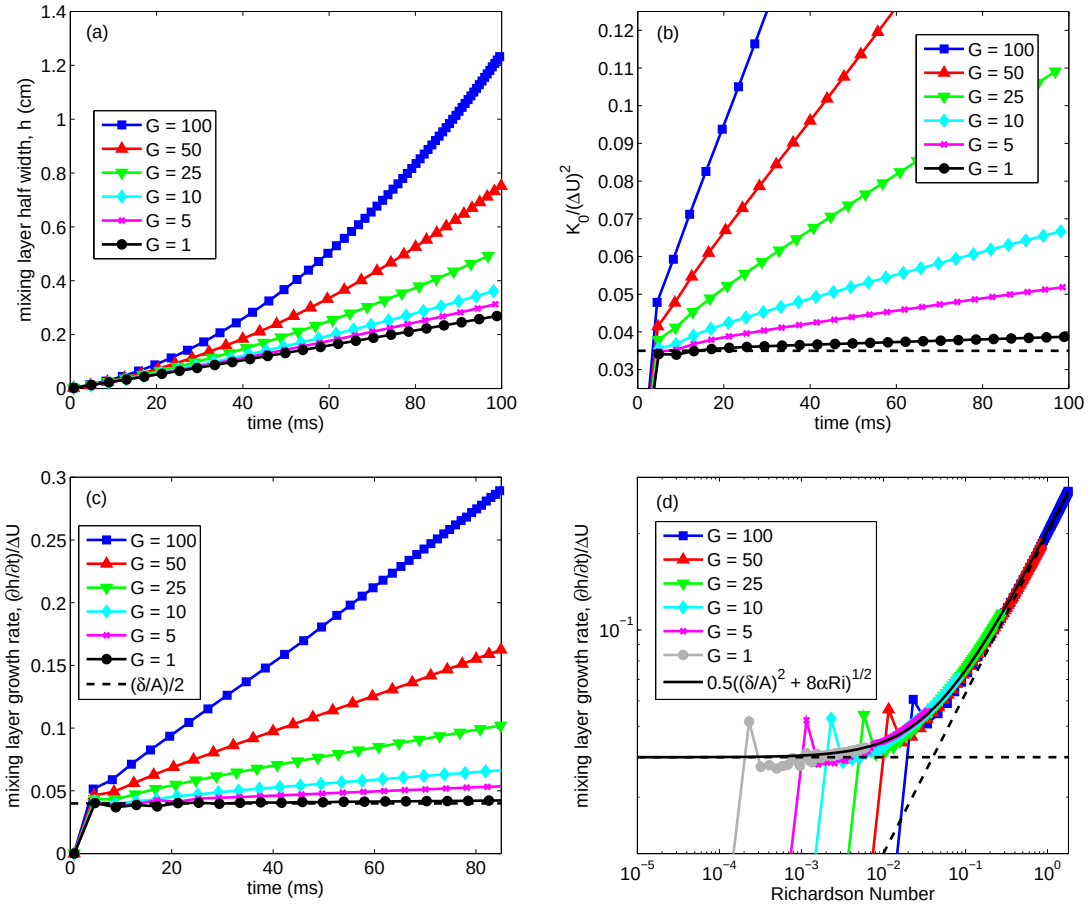

FIG. 11. Four measures of mixing layer and turbulence intensity evolution for k-$2L$-a simulations of combined RT/KH instability with increasing gravitational acceleration: (a) mixing layer half-width as a function of time, (b) turbulence intensity Φ^{-1} as a function of time, (c) the nondimensional growth rate $\dot{h}/\Delta U$ as a function of time, and (d) nondimensional growth rate as a function of Richardson number.

widths, then for the combined RT/KH mixing layer [50]

$$h = \alpha_b \, A \, g \, t^2 + \frac{\delta}{\mathcal{A}} \frac{\Delta U}{2} \, t \, . \tag{53}$$

If the mixing layer growth can be expressed by Eq. (53), then it is straightforward to derive

$$\frac{2\,\dot{h}}{\Delta U} = \sqrt{\left(\frac{\delta}{\mathcal{A}}\right)^2 + 8\,\alpha_b \,\mathrm{Ri}} \, . \tag{54}$$

for the nondimensional mixing layer growth rate as a function of Richardson number.

Figure 11 illustrates the mixing layer evolution as a function of time and Richardson number for each of the six cases shown in Fig. 10. First, in Fig. 11(a), the mixing layer half-width is plotted as a function of time. As the gravitational multiplier G is increased from 1 to 100, the evolution of h changes from a nearly linear function to what appears to be a quadratic function; such behavior is consistent with expectations of simulations in the KH and RT limits, respectively. Figure 11(b) shows the turbulence intensity, Φ^{-1}, as a function of time for each of the six cases. The expected KH value 0.035 is plotted for reference. It is clear that for all six cases, Φ^{-1} is increasing with time, as expected for an RT mixing layer. In the case of the lowest gravitational acceleration, however, the value does not rise much above the KH value 0.035, indicating that the $G = 1$ case stays mostly in the KH limit. Figure 11(c) shows the nondimensionalized mixing layer growth rate, $\dot{h}/\Delta U$ as a function of time; the expected KH value $(\delta/\mathcal{A})/2 = 0.04$ is also plotted for reference. This plot clearly indicates that the lowest acceleration case has a nearly constant growth rate close to the KH limit, while the higher acceleration cases demonstrate linearly increasing growth rates, as expected of mixing in the RT limit. Finally, in Fig. 11(d), nondimensionalized mixing layer growth rates are plotted as a function of Richardson number for the six cases. All six cases collapse along a common trajectory. Moreover, the relationship given in Eq. (54) is over-plotted in gray and appears to describe the behavior well, which implies that the realized growth rate predicted by the k-$2L$-a model is, in fact, a linear combination of the RT and KH growth rates.

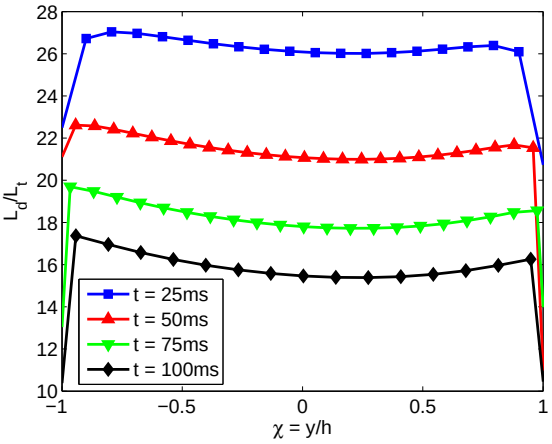

FIG. 12. The ratio of length scales L_d/L_t at four different times across a combined RT/KH mixing layer for $G = 10$.

Dashed lines in this plot indicate expected growth rates for RT and KH mixing layers in isolation. By observing where the simulations deviate from these reference lines, the space can be divided into KH-dominated mixing for $\mathrm{Ri} \lesssim 0.01$, RT-dominated mixing for $\mathrm{Ri} \gtrsim 0.25$, and transitional mixing for $0.01 < \mathrm{Ri} < 0.25$. These ranges are in reasonable agreement with experimental results by Akula *et al.* [52], who observe the transition point to RT-dominated mixing occurring for $\mathrm{Ri} = 0.17$–0.56.

Finally, Fig. 12 shows the ratio of length scales L_d/L_t across the combined RT/KH mixing layer at four different times for $G = 10$. In contrast to the flat profiles observed for canonical RT and KH mixing layers, the profile for combined RT/KH mixing demonstrates some curvature. Additionally, as the mixing layer evolves in time, the magnitude of the ratio is decreasing. Such behavior is consistent with the ratio transitioning from a value associated with KH-dominated mixing to a value of unity associated with RT-dominated mixing.

V. SUMMARY AND CONCLUSIONS

In the present work, the k-L-a model [48] has been extended by the addition of a second length scale equation similar to Schwarzkopf *et al* [57]. This enhancement has been shown to greatly improve prediction of shear-driven mixing without negative impact on the prediction of buoyancy-driven mixing. Constraints on model coefficients are derived which are necessary to satisfy an ansatz of self-similarity and to reproduce important experimental RT, RM, and KH growth parameters. Through application of the k-$2L$-a model to quasi-1D simulations of canonical buoyancy- and shear-driven mixing layers, it was demonstrated that, when model coefficients are specified according to constraints derived from self-similarity analysis, the expected growth parameters are recovered and good agreement is obtained in comparisons with experimental and LES data. Moreover, it was shown that in the absence of a second length scale equation, when model coefficients are set according to self-similarity constraints, it is not possible for the k-L-a model to simultaneously match desired KH turbulence intensity and growth parameters. Finally, by applying the model to simulations of combined RT/KH mixing, it was demonstrated that the mixing layer growth predicted by the model is a linear combination of the individual RT and KH growth, resulting in a simple relationship for the growth rate as a function of Richardson number. This relationship divides the combined RT/KH mixing evolution into KH-dominated mixing for $\mathrm{Ri} \lesssim 0.01$, RT-dominated mixing for $\mathrm{Ri} \gtrsim 0.25$, and transitional mixing for $0.01 < \mathrm{Ri} < 0.25$.

Although the present work has focused on simple, one-dimensional validation problems to calibrate and evaluate the two-length-scale model, further work remains to assess model predictions in more complicated multidimensional problems. Simulation of complex problems like the shock-shear experiments at the NIF and the OMEGA laser [53, 54] will require robust model predictions that remains to be demonstrated in more than one dimension. However, as the present work has shown, when the k-$2L$-a model is applied to problems of combined buoyancy- and shear-driven instability, the model is designed to reproduce expected growth parameters in the limits of both RT and KH mixing. Therefore, it is reasonable to expect sensible behavior when applied to more complicated problems.

ACKNOWLEDGMENTS

The authors thank Peter Rambo, Mark Ulitsky, and others at LLNL for helpful input and discussions. Tucker Hartland gratefully acknowledges support from the 2016 and 2017 LLNL High Energy Density Physics Summer Program. This work was performed under the auspices of the U.S. Department of Energy by Lawrence Livermore National Laboratory under Contract No. DE-AC52-07NA27344.

Appendix A: Self-similarity analysis for buoyancy- and shock-driven instability

This Appendix provides a derivation of self-similarity constraints for the k-$2L$-a model for canonical RT and RM mixing. It is included here for completeness; however, it should be noted that the constraints obtained herein do not significantly differ from those obtained for the single-length-scale k-L-a model [56]. Indeed, as the analysis in this Appendix will show, when self-similarity constraints are applied for canonical RT and RM mixing, the k-$2L$-a model reduces to the single-length-scale k-L-a model.

1. Self-similarity of the L_t equation

To begin, a change of variable is introduced in terms of the mixing layer half-width, $h(t)$. Let $\chi \equiv x/h$. It is assumed that k, L_t, and L_d are separable in space and time such that $k\,(\chi,t) = K_0(t) f(\chi)$, $L_t\,(\chi,t) = L_{t0}(t)\sqrt{f(\chi)}$, and $L_d\,(\chi,t) = L_{d0}(t)\sqrt{f(\chi)}$ with $f(\chi) = 1-\chi^2$. Applying the simplifying assumptions and substituting into Eq. (9) gives

$$\frac{D}{Dt}\left(L_{t0} f^{1/2}\right) = \frac{\partial}{\partial x}\left[\frac{C_\mu}{N_{Lt}} L_{t0} f \sqrt{2K_0}\,\frac{\partial}{\partial x}\left(L_{t0} f^{1/2}\right)\right] + C_{L1} f^{1/2}\sqrt{2K_0}\,. \tag{A1}$$

The self-similarity ansatz is applied by assuming that $L_{t0}(t) = \beta h(t)$. Equation (A1) is then transformed further to

$$\dot{L}_{t0} = \sqrt{2K_0}\left(C_{L1} - \frac{C_\mu}{N_{Lt}}\beta^2\right) + \sqrt{2K_0}\left(2\frac{C_\mu}{N_{Lt}}\beta^2 - C_{L1}\right)\left(\frac{x}{h}\right)^2 . \tag{A2}$$

In order to eliminate the spatial dependence on the right-hand side, $2\beta^2 = C_{L1} N_{Lt}/C_\mu$. Substituting this constraint into Eq. (A2) gives

$$\dot{L}_{t0}(t) = \frac{C_{L1}}{2}\sqrt{2K_0}\,. \tag{A3}$$

2. Self-similarity of the L_d equation

Applying the simplifying assumptions and substituting into Eq. (10) gives

$$\frac{D}{Dt}\left(L_{d0} f^{1/2}\right) = \frac{\partial}{\partial x}\left[\frac{C_\mu}{N_{Ld}} L_{t0} f \sqrt{2K_0}\,\frac{\partial}{\partial x}\left(L_{d0} f^{1/2}\right)\right] + C_{L1} f^{1/2}\sqrt{2K_0}\,. \tag{A4}$$

Applying the self-similarity ansatz further transforms Eq. (A4) to

$$\left(\dot{L}_{t0}\frac{L_{d0}}{L_{t0}} - \dot{L}_{d0}\right)\chi^2 + \dot{L}_{d0} = \sqrt{2K_0}\left(C_{L1} - \frac{C_\mu}{N_{Ld}}\frac{L_{d0}}{L_{t0}}\beta^2\right) + \sqrt{2K_0}\left(2\frac{C_\mu}{N_{Ld}}\frac{L_{d0}}{L_{t0}}\beta^2 - C_{L1}\right)\chi^2 . \tag{A5}$$

To satisfy the self-similarity ansatz requires

$$\dot{L}_{d0} = \sqrt{2K_0}\left(C_{L1} - \frac{C_\mu}{N_{Ld}}\frac{L_{d0}}{L_{t0}}\beta^2\right), \tag{A6}$$

$$\dot{L}_{t0}\frac{L_{d0}}{L_{t0}} - \dot{L}_{d0} = \sqrt{2K_0}\left(2\frac{C_\mu}{N_{Ld}}\frac{L_{d0}}{L_{t0}}\beta^2 - C_{L1}\right). \tag{A7}$$

Substituting Eq. (A3) into Eq. (A7) yields the constraint

$$N_{Lt} = N_{Ld}\,. \tag{A8}$$

Eliminating the spatial dependence requires

$$\frac{L_{d0}}{L_{t0}} = \frac{N_{Ld}}{N_{Lt}} = 1\,, \tag{A9}$$

and Eq. (A5) reduces to

$$\dot{L}_{d0}(t) = \frac{C_{L1}}{2}\sqrt{2K_0}\,. \tag{A10}$$

3. Self-similarity of the a equation

Consider an RT-unstable configuration of two fluids in hydrostatic equilibrium with gravitational acceleration. Equation (11) transforms to

$$\rho\,\frac{Da}{Dt} = \frac{\partial}{\partial x}\left(\frac{\mu_t}{N_a}\,\frac{\partial a}{\partial x}\right) - C_B^2\,\rho\,g\,b - \rho\,C_a\,a\,\frac{(2\,k)^{1/2}}{L_d} - \frac{2}{3}\,k\,\frac{\partial \rho}{\partial x}\,. \tag{A11}$$

Assume that the mean density profile is given in terms of the density of the heavy fluid, ρ_H, and the density of the light fluid, ρ_L. Then, the self-similar density profile is

$$\rho = \rho_0\left(1 + A\frac{x}{h}\right), \tag{A12}$$

where ρ_0 indicates the density at $x = 0$, and A is the conventional Atwood number:

$$\rho_0 = \frac{\rho_H + \rho_L}{2} \quad \text{and} \quad A = \frac{\rho_H - \rho_L}{\rho_H + \rho_L}\,. \tag{A13}$$

Substituting into Eq. (14) gives the self-similar form

$$b = \frac{A^2}{1-A^2}\,f\,. \tag{A14}$$

Also assume the self-similar form

$$a = -C_B\,\frac{A}{1-A^2}\,\sqrt{2\,K_0}\,f\,. \tag{A15}$$

Substituting Eqs. (A12)–(A15) into Eq. (A11) yields

$$\left[\frac{\dot{K}_0}{\sqrt{2K_0}}+\frac{C_{L1}N_{Lt}}{N_a}\frac{(2K_0)}{L_{t0}}-C_BAg+\left(C_a-\frac{\beta}{3C_B}\right)\frac{2K_0}{L_{t0}}\right]-$$
$$\left[\frac{\dot{K}_0}{\sqrt{2K_0}}+\left(\frac{3C_{L1}N_{Lt}}{N_a}-C_{L1}\right)\frac{(2K_0)}{L_{t0}}-C_BAg+\left(C_a-\frac{\beta}{3C_B}\right)\frac{2K_0}{L_{t0}}\right]\chi^2=0 \tag{A16}$$

after collecting terms and rearranging. For the self-similarity ansatz to be satisfied, the χ^2 terms must go to zero, which requires $N_a = 2N_{Lt}$. Applying this condition and introducing the change of variable $V_0 \equiv \sqrt{2K_0}$ reduces Eq. (A16) to

$$\dot{V}_0 = C_BAg - \frac{V_0^2}{L_{t0}}\left(C_a-\frac{\beta}{3C_B}+\frac{C_{L1}}{2}\right). \tag{A17}$$

4. Self-similarity of the k equation

Considering the RT-unstable problem in hydrostatic equilibrium, Eq. (8) may be transformed to

$$\frac{Dk}{Dt} = \frac{\partial}{\partial x}\left(\frac{C_\mu L_{t0} f\sqrt{2K_0}}{N_k}\frac{\partial k}{\partial x}\right) + g\,C_B\,\frac{A}{1-A^2}\,\sqrt{2\,K_0}\,f - C_D\,\frac{(2k)^{3/2}}{L}. \tag{A18}$$

After substituting for k, expanding the material derivative, and collecting terms, Eq. (A18) is reduced to

$$\left[\dot{K}_0+\frac{C_{L1}N_{Lt}}{2N_k}\frac{(2K_0)^{3/2}}{L_{t0}}-C_BAg\sqrt{2K_0}+C_D\frac{(2K_0)^{3/2}}{L_{d0}}\right]-$$
$$\left[\dot{K}_0+\left(\frac{3C_{L1}N_{Lt}}{2N_k}-\frac{C_{L1}}{2}\right)\frac{(2K_0)^{3/2}}{L_{t0}}-C_BAg\sqrt{2K_0}+C_D\frac{(2K_0)^{3/2}}{L_{t0}}\right]\chi^2=0\,. \tag{A19}$$

For the self-similarity ansatz to be satisfied, the χ^2 terms must go to zero, which requires $N_k = 2N_{Lt}$. Applying this condition and introducing the change of variable $V_0 \equiv \sqrt{2K_0}$ reduces Eq. (A19) to

$$\dot{V}_0 = C_B\,A\,g - \frac{V_0^2}{L_{t0}}\left(C_D+\frac{C_{L1}}{4}\right). \tag{A20}$$

In order to simultaneously satisfy Eqs. (A17) and (A20) requires

$$C_a = C_D + \frac{\beta}{3\,C_B} - \frac{C_{L1}}{4}\,. \tag{A21}$$

5. Richtmyer–Meshkov growth exponent

Experimental observations are now utilized to provide further constraints. In an RM configuration, after the shock has passed, the acceleration term in Eq. (A20) vanishes. Substitution of Eq. (A10) into Eq. (A20) gives

$$\frac{2}{C_{L1}}\ddot{L}_{d0} = -2\frac{\dot{L}_{d0}^2}{L_{d0}}\left(\frac{C_D}{C_{L1}}+\frac{1}{4}\right). \tag{A22}$$

Integrating this equation for L_{d0} requires initial values of $L_{d0}(0)$ and $\dot{L}_{d0}(0)$. Anticipating the result, substituting a solution of the form

$$L_{d0}(t) = L_{d0}(0)\left[\frac{\dot{L}_{d0}(0)}{\theta L_{d0}(0)}t+1\right]^\theta \tag{A23}$$

and its derivatives into Eq. (A22) gives an expression which may be rearranged to provide a constraint on the ratio C_D/C_{L1} in terms of the RM growth exponent θ:

$$\frac{C_D}{C_{L1}} = \frac{2-3\,\theta}{4\,\theta}\,. \tag{A24}$$

6. Rayleigh–Taylor growth parameter

In an RT configuration, the acceleration term in Eq. (A20) cannot be neglected. Substituting a solution of the form $L_{d0} = BAgt^2$ into Eq. (A10) gives $V_0 = (4/C_{L1})\,BAgt$. Substituting the trial solutions into Eq. (A20) provides a relationship between the RT con-

stant B and the model coefficients,

$$B = \frac{C_B\, C_{L1}}{8\left(1 + 2\,\frac{C_D}{C_{L1}}\right)}\,. \tag{A25}$$

For small Atwood number the bubble height should grow according to $h(t) = \alpha_b g A t^2$, so that

$$h(t) = \frac{L_{d0}(t)}{\beta} = \sqrt{\frac{C_\mu\, C_{L1}}{N_k}}\,\frac{C_B}{4\left(1 + 2\,\frac{C_D}{C_{L1}}\right)}\,A\,g\,t^2,$$

$$C_B = \frac{4\,\alpha_b\left(1 + 2\,\frac{C_D}{C_{L1}}\right)}{\sqrt{\frac{C_\mu\, C_{L1}}{N_k}}}\,. \tag{A26}$$

The kinetic energy generated within an RT mixing layer is

$$\begin{aligned} E_K &= \int_{-h}^{h} \rho\, K(x,t)\,\mathrm{d}x \\ &= K_0 \int_{-h}^{h} \left(\rho_0 + \frac{\partial \rho}{\partial x}\,x\right)\left[1 - \left(\frac{x}{h}\right)^2\right]\mathrm{d}x \\ &= K_0 \int_{-h}^{h} \rho_0 \left[1 - \left(\frac{x}{h}\right)^2\right] + \frac{\partial \rho}{\partial x}\left(x - \frac{x^3}{h^2}\right)\mathrm{d}x\,. \end{aligned} \tag{A27}$$

By symmetry, the integral over odd powers of x will vanish, leaving $E_K = (4/3)h(t)\rho_0 K_0(t)$. As K_0/L_{d0} is constant, K_0/h should also be constant, which allows further reduction:

$$\frac{K_0}{h} = \beta\,\frac{K_0}{L_{d0}} = \frac{2\,\alpha_b\, A\, g\, N_k}{C_{L1}\, C_\mu}, \tag{A28}$$

$$E_K = \frac{8}{3}\,\frac{N_k}{C_{L1}\, C_\mu}\,\alpha_b\, A\,\rho_0\, g\, h^2\,. \tag{A29}$$

The gravitational potential energy within an RT mixing layer can also be derived by assuming a material interface at $x = 0$ and integrating over a distance $2d$,

$$\begin{aligned} \mathrm{PE} &= -g \int_{-d}^{d} \rho(x)\, x\,\mathrm{d}x \\ &= -\frac{g}{2}\,(\rho_H - \rho_L)\, d^2 + \frac{g}{6}\,(\rho_H - \rho_L)\, h^2\,. \end{aligned} \tag{A30}$$

As only the change in potential energy over the mixing layer is relevant, consider the term proportional to h, $\Delta\mathrm{PE} = (g/6)\,(\rho_H - \rho_L)\, h^2$. Thus, the fraction of potential energy converted to kinetic energy is

$$\frac{E_K}{\Delta\mathrm{PE}} = \frac{\frac{8}{3}\,\frac{N_k}{C_{L1}\, C_\mu}\,\alpha_b\, A\frac{\rho_H + \rho_L}{2}\, g\, h^2}{\frac{g}{6}\,(\rho_H - \rho_L)\, h^2} = \frac{8\, N_k\, \alpha_b}{C_{L1}\, C_\mu}\,. \tag{A31}$$

7. Self-Similarity of the scalar equation

Conservation of species mass fraction in one dimension is expressed by

$$\frac{DY}{Dt} = \frac{\partial}{\partial x}\left(\frac{C_\mu\, L\,\sqrt{2\,k}}{N_Y}\,\frac{\partial Y}{\partial x}\right)\,, \tag{A32}$$

where the species subscript on the mass fraction has been dropped for simplicity. It is assumed that the self-similar solution for the light fluid is $Y(x,t) = 0.5\,[1 - x/h(t)]$ with derivatives

$$\frac{\partial Y}{\partial t} = \frac{x\,\dot{h}}{2\,h^2} \quad , \quad \frac{\partial Y}{\partial x} = -\frac{1}{2\,h}\,. \tag{A33}$$

It is additionally useful to write

$$\begin{aligned} \sqrt{2\,k(x,t)} &= \sqrt{2\,K_0(t)}\sqrt{1 - \left(\frac{x}{h}\right)^2} \\ &= \frac{2}{C_{L1}}\,\dot{L}_{t0}(t)\,\sqrt{1 - \left(\frac{x}{h}\right)^2}\,. \end{aligned} \tag{A34}$$

Substituting Eqs. (A33) and (A34) into Eq. (A32) gives

$$\dot{Y} = \frac{x\,\dot{h}}{2\,h^2} = \frac{2\,C_\mu}{C_{L1}\, N_Y}\,\frac{L_{t0}\,\dot{L}_{t0}\,x}{h^3}\,. \tag{A35}$$

Finally, using $L_{t0} = \beta h$ and $\dot{L}_{t0} = \beta\dot{h}$ and substituting into Eq. (A35) gives

$$\dot{Y} = \frac{x\,\dot{h}}{2\,h^2} = \frac{N_{Lt}}{N_Y}\,\frac{x\,\dot{h}}{h^2}\,. \tag{A36}$$

This equation can only be satisfied if $N_Y = 2N_{Lt}$.

8. Self-Similarity of the internal energy equation

Applying the simplifying assumptions and substituting into Eq. (7) gives

$$\frac{De}{Dt} = \frac{\partial}{\partial x}\left(\frac{C_\mu\, L_t\,\sqrt{2\,k}}{N_e}\,\frac{\partial e}{\partial x}\right) + C_D\,\frac{(2\,k)^{3/2}}{L_d}\,. \tag{A37}$$

It is assumed that the self-similar solution takes form $e(x,t) = e_0 + e_1 f(x,t)$. After some algebra and substitution,

$$\begin{aligned} \frac{e_1\, C_{L1}\, V_0}{L_{t0}}\,\chi^2 = &-\frac{N_{Lt}}{N_e}\,\frac{e_1\, C_{L1}\, V_0}{L_{t0}}\left(1 - 3\chi^2\right) \\ &+ C_D\,\frac{V_0^3}{L_{t0}}\left(1 - \chi^2\right)\,. \end{aligned} \tag{A38}$$

To satisfy the self-similarity ansatz, the spatial dependence must drop out. Considering first the terms without spatial dependence gives

$$-\frac{N_{Lt}}{N_e}\,\frac{e_1\, C_{L1} V_0}{L_{t0}} + C_D\,\frac{V_0^3}{L_{t0}} = 0 \tag{A39}$$

which can be rearranged to give

$$C_D\, V_0^2 = \frac{e_1\, C_{L1}\, N_{Lt}}{N_e}\,. \tag{A40}$$

Utilizing Eq. (A40) provides an expression for the χ terms,

$$\frac{e_1\, C_{L1}\, V_0}{L_{t0}} = \frac{2\, N_{Lt}}{N_e}\,\frac{e_1\, C_{L1}\, V_0}{L_{t0}}\,, \tag{A41}$$

which can only be satisified if $N_e = 2N_{Lt}$.

Appendix B: Stress-limiter modification

The inclusion of the L_t/k and L_d/k terms in Eqs. (9) and (10) can lead to numerical instability and sensitivity to intial conditions when k is at or near zero. Division by small value can potentially be avoided, if these terms are expanded and re-written in terms of the turbulence transport and destruction time scales, T_t and T_d:

$$\begin{aligned}\overline{\rho}\frac{DL_t}{Dt} =& C_{L1}\overline{\rho}\sqrt{2k} + \frac{\partial}{\partial x_i}\left(\frac{\mu_t}{N_{Lt}}\frac{\partial L_t}{\partial x_i}\right)\\ &+C_{L2t}\overline{\rho}\left(2C_{dev}C_\mu T_t L_t \widetilde{S}_{ij} - \frac{2}{3}L_t\delta_{ij}\right)\frac{\partial \widetilde{u}_i}{\partial x_j}\end{aligned} \tag{B1}$$

$$\begin{aligned}\overline{\rho}\frac{DL_d}{Dt} =& C_{L1}\overline{\rho}\sqrt{2k} + \frac{\partial}{\partial x_i}\left(\frac{\mu_t}{N_{Ld}}\frac{\partial L_d}{\partial x_i}\right)\\ &+C_{L2d}\overline{\rho}\left(2C_{dev}C_\mu T_d L_t \widetilde{S}_{ij} - \frac{2}{3}L_d\delta_{ij}\right)\frac{\partial \widetilde{u}_i}{\partial x_j}\,,\end{aligned} \tag{B2}$$

where

$$\mu_t = C_\mu\, \overline{\rho}\, k\, T_t\,, \tag{B3}$$

and the limited time scales are

$$T_t = \min\left(\frac{L_t}{\sqrt{2\,k}},\, \frac{1}{3\,C_\mu\,\sqrt{2\,\widetilde{S}_{ij}\,\widetilde{S}_{ij}}}\right), \tag{B4}$$

$$T_d = \min\left(\frac{L_d}{\sqrt{2\,k}},\, \frac{1}{3\,C_\mu\,\sqrt{2\,\widetilde{S}_{ij}\,\widetilde{S}_{ij}}}\right). \tag{B5}$$

By formulating the eddy viscosity in this way, realizability is enforced by invoking the constraint that the eigenvalues, λ_α, of the strain-rate tensor must satisfy [66]

$$|\lambda_\alpha| \le \sqrt{\widetilde{S}_{ij}\,\widetilde{S}_{ij}/2} \quad , \quad 2\,\frac{\mu_t}{\overline{\rho}}\max_\alpha \lambda_\alpha \le \frac{2}{3}\,k\,. \tag{B6}$$

As discussed in Section III C, however, L_d is expected to be strictly greater than L_t. It may therefore be insufficient to limit T_t alone. Instead, both T_t and T_d are limited by the time scale associated with the mean strain. As discussed in Section IV C, when limiting is applied in this manner, it reduces growth rate overshoot and duration of transience in simulations with strong shear.

[1] Lord Rayleigh, "Investigation of the character of the equilibrium of an incompressible heavy fluid of variable density," Proc. R. Math. Soc. **14**, 170–177 (1883).

[2] G. I. Taylor, "The instability of liquid surfaces when accelerated in a direction perpendicular to their plane," Proc. R. Soc. London A **201**, 192–196 (1950).

[3] R. D. Richtmyer, "Taylor instability in shock acceleration of compressible fluids," Commun. Pure Appl. Math **8**, 297–319 (1960).

[4] E. E. Meshkov, "Instability of the interface of two gases accelerated by a shock wave," Sov. Fluid Dyn. **4**, 101–108 (1969).

[5] M. Brouillette, "The Richtmyer-Meshkov instability," Annu. Rev. Fluid Mech. **34**, 445–468 (2002).

[6] J. Yang, T. Kubota, and E. E. Zukoski, "Applications of shock-induced mixing to supersonic combustion," AIAA J. **31**, 854–862 (1993).

[7] D. Arnett, "The role of mixing in astrophysics," Ap. J. Suppl. **127**, 213–217 (2000).

[8] J. D. Lindl, R. L. McCrory, and E. M. Campbell, "Progress toward ignition and burn propagation in inertial confinement fusion," Physics Today **45**, 32–40 (1992).

[9] Sir W. Thomson F.R.S. (Lord Kelvin), "XLVI. Hydrokinetic solutions and observations," Philosophical Magazine **42**, 362–377 (1871).

[10] H. Helmholtz, "XLIII. On discontinuous movements of fluids," Philosophical Magazine **36**, 337–346 (1868).

[11] F. K. Browand and C. D. Winant, "Laboratory observations of shear-layer instability in a stratified fluid," Boundary-Layer Meteorol. **5**, 67–77 (1973).

[12] I. P. D. De Silva, H. J. S. Fernando, F. Eaton, and D. Hebert, "Evolution of Kelvin-Helmholtz billows in nature and laboratory," Earth Planet. Sci. Lett. **143**, 217–231 (1996).

[13] J. Werne and D. C. Fritts, "Stratified shear turbulence: Evolution and statistics," Geophys. Res. Lett. **26**, 703–711 (1999).

[14] M. C. Kelley, C. Y. Chen, R. R. Beland, R. Woodman, J. L. Chau, and J. Werne, "Resistance of a Kelvin-Helmholtz instability in the upper troposphere," J. Geophys. Res. **110**, 1–7 (2005).

[15] K. O. Mikaelian, "Oblique shocks and the combined

Rayleigh-Taylor, Kelvin-Helmholtz, and Richtmyer-Meshkov instabilities," Phys. Fluids **6**, 1943–1945 (1994).
[16] J. A. McFarland, J. A. Greenough, and D. Ranjan, "Computational parametric study of a Richtmyer-Meshkov instability for an inclined interface," Phys. Rev. E **84**, 026303 (2011).
[17] G. L. Brown and A. Roshko, "On density effects and large structure in turbulent mixing layers," J. Fluid Mech. **64**, 775–816 (1974).
[18] J. H. Bell and R. D. Mehta, "Development of a two-stream mixing layer from tripped and untripped boundary layers," AIAA J. **28**, 2034–2042 (1990).
[19] M. Vetter and B. Sturtevant, "Experiments on the Richtmyer-Meshkov instability of an air/SF_6 interface," Shock Waves **4**, 247–252 (1995).
[20] M. Schneider, G. Dimonte, and B. Remington, "Large and small scale structure in Rayleigh-Taylor mixing," Phys. Rev. Lett. **80**, 3507–3510 (1998).
[21] G. Dimonte and M. Schneider, "Density ratio dependence of Rayleigh-Taylor mixing for sustained and impulsive acceleration histories," Phys. Fluids **12**, 304–321 (2000).
[22] S. B. Dalziel, P. F. Linden, and D. L. Youngs, "Self-similarity and internal structure of turbulence induced by Rayleigh-Taylor instability," J. Fluid Mech. **399**, 1–48 (1999).
[23] P. Ramaprabhu and M. J. Andrews, "Experimental investigation of Rayleigh-Taylor mixing at small Atwood numbers," J. Fluid Mech. **502**, 233–271 (2004).
[24] J. W. Jacobs and S. B. Dalziel, "Rayleigh-Taylor instability in complex stratifications," J. Fluid Mech. **542**, 251–279 (2005).
[25] N. J. Mueschke, M. J. Andrews, and O. Schilling, "Experimental characterization of initial conditions and spatio-temporal evolution of a small-Atwood-number Rayleigh–Taylor mixing layer," J. Fluid Mech. **567**, 27–63 (2006).
[26] N. J. Mueschke, O. Schilling, D. L. Youngs, and M. J. Andrews, "Measurements of molecular mixing in a high-Schmidt-number Rayleigh–Taylor mixing layer," J. Fluid Mech. **632**, 17–48 (2009).
[27] D. H. Olson and J. W. Jacobs, "Experimental study of Rayleigh-Taylor instability with a complex initial perturbation," Phys. Fluids **21**, 034103 (2009).
[28] E. Leinov, G. Malamud, Y. Elbaz, L. A. Levin, G. Ben-Dor, D. Shvarts, and O. Sadot, "Experimental and numerical investigation of the Richtmyer–Meshkov instability under re-shock conditions," J. Fluid Mech. **626**, 449–475 (2009).
[29] A. Banerjee, W. N. Kraft, and M. J. Andrews, "Detailed measurements of a statistically steady Rayleigh-Taylor mixing layer from small to high Atwood numbers," J. Fluid Mech. **659**, 127–190 (2010).
[30] A. W. Cook and P. E. Dimotakis, "Transition stages of Rayleigh-Taylor instability between miscible fluids," J. Fluid Mech. **443**, 69–99 (2001).
[31] A. W. Cook, W. Cabot, and P. L. Miller, "The mixing transition in Rayleigh–Taylor instability," J. Fluid Mech. **511**, 333–362 (2004).
[32] W. H. Cabot and A. W. Cook, "Reynolds number effects on Rayleigh-Taylor instability with possible implications for type Ia supernovae," Nature Phys. **2**, 562–568 (2006).
[33] J. R. Ristorcelli and T. T. Clark, "Rayleigh–Taylor turbulence: self-similar analysis and direct numerical simulation," J. Fluid Mech. **507**, 213–253 (2004).
[34] P. Ramaprabhu, G. Dimonte, and M. J. Andrews, "A numerical study of the influence of initial perturbations on the turbulent Rayleigh-Taylor instability," J. Fluid Mech. **536**, 285–319 (2005).
[35] O. Schilling, M. Latini, and W. S. Don, "Physics of reshock and mixing in single-mode Richtmyer-Meshkov instability," Phys. Rev. E **76**, 026319 (2007).
[36] N. Vladimirova and M. Chertkov, "Self-similarity and universality in Rayleigh-Taylor, Boussinesq turbulence," Phys. Fluids **21**, 015102 (2009).
[37] N. J. Mueschke and O. Schilling, "Investigation of Rayleigh–Taylor turbulence and mixing using direct numerical simulation with experimentally measured initial conditions. I. Comparison to experimental data," Phys. Fluids **21**, 014106 (2009).
[38] N. J. Mueschke and O. Schilling, "Investigation of Rayleigh–Taylor turbulence and mixing using direct numerical simulation with experimentally measured initial conditions. II. Dynamics of transitional flow and mixing statistics," Phys. Fluids **21**, 014107 (2009).
[39] O. Schilling and M. Latini, "High-order WENO simulations of three-dimensional reshocked Richtmyer–Meshkov instability to late times: Dynamics, dependence on initial conditions, and comparisons to experimental data," Acta Mech. Scientia **30B**, 595–620 (2010).
[40] O. Schilling and N. J. Mueschke, "Analysis of turbulent transport and mixing in transitional Rayleigh–Taylor unstable flow using direct numerical simulation data," Phys. Fluids **22**, 105102 (2010).
[41] D. Livescu, J. R. Ristorcelli, M. R. Petersen, and R. A. Gore, "New phenomena in variable-density Rayleigh-Taylor turbulence," Phys. Scr. **T146**, 014015 (2010).
[42] G. Boffetta, A. Mazzino, S. Musacchio, and L. Vozella, "Statistics of mixing in three-dimensional Rayleigh-Taylor turbulence at low Atwood number and Prandtl number one," Phys. Fluids **22**, 035109 (2010).
[43] O. Soulard and J. Griffond, "Inertial-range anisotropy in Rayleigh-Taylor turbulence," Phys. Fluids **24**, 025101 (2012).
[44] C. Cambon and B.-J. Gréa, "The role of directionality on the structure and dynamics of strongly anisotropic turbulent flows," J. Turbul. **14**, 50–71 (2013).
[45] B. J. Olson and J. Greenough, "Large eddy simulation requirements for the Richtmyer-Meshkov instability," Phys. Fluid **26**, 044103 (2014).
[46] V. K. Tritschler, B. J. Olson, S. K. Lele, S. Hickel, X. Y. Hu, and N. A. Adams, "On the Richtmyer-Meshkov instability evolving from a deterministic multimode planar interface," J. Fluid Mech. **755**, 429–462 (2014).
[47] B. Thornber, "Impact of domain size and statistical errors in simulations of homogeneous decaying turbulence and the Richtmyer-Meshkov instability," Phys. Fluids **28**, 045106 (2016).
[48] B. E. Morgan, B. J. Olson, J. E. White, and J. A. McFarland, "Self-similarity of a Rayleigh-Taylor mixing layer at low Atwood number with a multimode initial perturbation," J. Turbul. **18**, 973–999 (2017).
[49] B. Thornber, J. Griffond, O. Poujade, N. Attal, H. Varshochi, P. Bigdelou, P. Ramaprabhu, B. Olson, J. Greenough, Y. Zhou, O. Schilling, K. A. Garside, R. J. R. Williams, C. A. Batha, P. A. Kuchugov, M. E. Ladonkina, V. F. Tishkin, N. V. Zmitrenko, V. B. Rozanov, and D. L. Youngs, "Late-time growth rate, mixing, and anisotropy in the multimode narrowband

richtmyer–meshkov instability: The θ-group collaboration," Phys. Fluids **29**, 105107 (2017).
[50] B. Akula, M. J. Andrews, and D. Ranjan, "Effect of shear on Rayleigh-Taylor mixing at small Atwood number," Phys. Rev. E **87**, 033013 (2013).
[51] B. Akula and D. Ranjan, "Dynamics of buoyancy-driven flows at moderately high Atwood numbers," J. Fluid Mech. **795**, 313–355 (2016).
[52] B. Akula, P. Suchandra, M. Mikhaeil, and D. Ranjan, "Dynamics of unstably stratified free shear flows: an experimental investigation of coupled Kelvin–Helmholtz and Rayleigh–Taylor instability," J. Fluid Mech. **816**, 619–660 (2017).
[53] F. W. Doss, J. L. Kline, K. A. Flippo, T. S. Perry, B. G. DeVolder, I. Tregellis, E. N. Loomis, E. C. Merritt, T. J. Murphy, L. Welser-Sherrill, and J. R. Fincke, "The shock/shear platform for planar radiation-hydrodynamics experiments on the National Ignition Facility," Phys. Plasmas **22**, 056303 (2015).
[54] F. W. Doss, J. R. Fincke, E. N. Loomis, L. Welser-Sherrill, and K. A. Flippo, "The high-energy-density counterpropagating shear experiment and turbulent self-heating," Phys. Plasmas **20**, 122704 (2013).
[55] B. J. Olson, J. Larsson, S. K. Lele, and A. W. Cook, "Nonlinear effects in the combined Rayleigh-Taylor/Kelvin-Helmholtz instability," Phys. Fluids **23**, 114107 (2011).
[56] B. E. Morgan and M. E. Wickett, "Three-equation model for the self-similar growth of Rayleigh-Taylor and Richtmyer-Meshkov instabilities," Phys. Rev. E **91**, 043002 (2015).
[57] J. D. Schwarzkopf, D. Livescu, J. R. Baltzer, R. A. Gore, and J. R. Ristorcelli, "A two-length scale turbulence model for single-phase multi-fluid mixing," Flow Turbul. Combust. **96**, 1–43 (2016).
[58] S. B. Pope, *Turbulent Flows* (Cambridge University Press, 2000).
[59] G. Dimonte, D. L. Youngs, A. Dimits, S. Weber, M. Marinak, S. Wunsch, C. Garasi, A. Robinson, M. J. Andrews, P. Ramaprabhu, A. C. Calder, B. Fryxell, J. Biello, L. Dursi, P. MacNeice, K. Olson, P. Ricker, R. Rosner, F. Timmes, H. Tufo, Y.-N. Young, and M. Zingale, "A comparative study of the turbulent Rayleigh-Taylor instability using high-resolution three-dimensional numerical simulations: The Alpha-Group collaboration," Phys. Fluids **16**, 1668–1693 (2004).
[60] D. Oron, L. Arazi, D. Kartoon, A. Rikanati, U. Alon, and D. Shvarts, "Dimensionality dependence of Rayleigh-Taylor and Richtmyer-Meshkov instability late-time scaling laws," Phys. Plasmas **8**, 2883 (2001).
[61] B. E. Morgan J. A. Greenough, "Large-eddy and unsteady RANS simulations of a shock-accelerated heavy gas cylinder," Shock Waves **26**, 355–383 (2016).
[62] B. J. Olson and J. Greenough, "Comparison of two- and three-dimensional simulations of miscible rychtmyer-meshkov instability with multimode initial conditions," Phys. Fluid **26**, 101702 (2014).
[63] G. Malamud, E. Leinov, O. Sadot, Y. Elbaz, G. Ben-Dor, and D. Shvarts, "Reshocked richtmyer-meshkov instability: Numerical study and modeling of random multimode experiments," Phys. Fluid **26**, 084107 (2014).
[64] J. T. Morán-López and O. Schilling, "Multicomponent Reynolds-averaged Navier–Stokes simulations of reshocked Richtmyer–Meshkov instability-induced mixing," High Energy Density Phys. **9**, 112–121 (2013).
[65] J. T. Morán-López and O. Schilling, "Multi-component Reynolds-averaged Navier–Stokes simulations of Richtmyer–Meshkov instability and mixing induced by reshock at different times," Shock Waves **24**, 325–343 (2014).
[66] P. A. Durbin, "On the k-3 stagnation point anomaly," Int. J. Heat and Fluid Flow **17**, 89–90 (1996).